Title

A framework for target discovery in rare cancers

Authors

Bingchen Li[1,‡], Ananthan Sadagopan[1,‡], Jiao Li[1], Yuqianxun Wu[1], Yantong Cui[1], Prathyusha Konda[1], Cary N. Weiss[1,2], Toni K. Choueiri[1,3,4], John G. Doench[5], Srinivas R. Viswanathan[1,3,4,5*]

Affiliations

[1]Department of Medical Oncology, Dana-Farber Cancer Institute; Boston, MA 02215, USA.

[2]Department of Pediatric Oncology, Dana-Farber Cancer Institute; Boston, MA 02215, USA.

[3]Department of Medicine, Harvard Medical School; Boston, MA 02215, USA.

[4]Department of Medicine, Brigham and Women's Hospital; Boston, MA 02215, USA.

[5]Broad Institute of MIT and Harvard; Cambridge, MA 02142, USA.

‡Authors contributed equally.

*To whom correspondence should be addressed: srinivas.viswanathan@dfci.harvard.edu (S.R.V)

Abstract

While large-scale functional genetic screens have uncovered numerous cancer dependencies, rare cancers are poorly represented in such efforts and the landscape of dependencies in many rare cancers remains obscure. We performed genome-scale CRISPR knockout screens in an exemplar rare cancer, *TFE3*-translocation renal cell carcinoma (tRCC), revealing previously unknown tRCC-selective dependencies in pathways related to mitochondrial biogenesis, oxidative metabolism, and kidney lineage specification. To generalize to other rare cancers in which experimental models may not be readily available, we employed machine learning to infer gene dependencies in a tumor or cell line based on its transcriptional profile. By applying dependency prediction to alveolar soft part sarcoma (ASPS), a distinct rare cancer also driven by *TFE3* translocations, we discovered and validated that *MCL1* represents a dependency in ASPS but not tRCC. Finally, we applied our model to predict gene dependencies in tumors from the TCGA (11,373 tumors; 28 lineages) and multiple additional rare cancers (958 tumors across 16 types, including 13 distinct subtypes of kidney cancer), nominating potentially actionable vulnerabilities in several poorly-characterized cancer types. Our results couple unbiased functional genetic screening with a predictive model to establish a landscape of candidate vulnerabilities across cancers, including several rare cancers currently lacking in potential targets.

Main Text

Introduction

A cornerstone of precision oncology is the matching of therapies to specific cancers based on predictive molecular features. Recent advances in the molecular classification of cancer coupled with advances in genome-scale functional genetic screening have enabled the discovery of multiple biomarker-drug pairs that have proven clinically effective in specific cancer subtypes (1–9). Still, limited molecular profiles of rare cancer types and a paucity of robust cellular models for many of these cancers remain barriers to fully realizing the ideal of precision oncology; this is in spite of the fact that many rare cancers have homogeneous genomic landscapes with singular driver alterations that may be directly linked to robust vulnerabilities (10–12).

Kidney cancer is notable in this regard as it comprises dozens of biologically distinct histologies in both adults and children, many of which are quite rare (13). To date, most discovery biology efforts in kidney cancer have focused on clear-cell renal cell carcinoma (ccRCC), which comprises 75% of RCC in adults and is typified by loss of the *VHL* tumor suppressor gene, leading to activation of hypoxia signaling (14). While therapeutic agents targeting this pathway have demonstrated promise in ccRCC (15), other RCC subtypes do not typically harbor *VHL* alterations and are driven by distinct biology (16). It is therefore likely that subtypes of kidney cancer differ in their dependency profiles, though this has not yet been systematically explored.

Translocation renal cell carcinoma (tRCC) is one such subtype of RCC that strikes both adults and children. Molecularly, tRCC is driven by an activating gene fusion involving an MiT/TFE family transcription factor, most commonly *TFE3* (17). Due to a lack of therapies specifically targeted to the biology of tRCC, therapies for ccRCC are frequently used; however, these yield poor response rates (18–23). The discovery of novel molecular targets in tRCC is therefore a pressing unmet need.

Recent studies have revealed few recurrent genomic alterations in tRCC apart from the driver fusion (23–28). Unbiased functional genetic screening can be useful for nominating vulnerabilities in such cases (11,12), but tRCC cell line models have not yet been included in large scale screening efforts (7,29–31), and only a limited number of cell line models of this cancer have been reported (17,32–34). In addition, *TFE3* fusions can drive a spectrum of other rare cancers apart from tRCC, including alveolar soft part sarcoma (ASPS) (35), perivascular epithelioid cell tumor (PEComa) (36), epithelioid haemangioendothelioma (EHE (37), malignant chondroid syringoma (38), and ossifying fibromyxoid tumors (39). It remains unknown whether these tumor types, most of which do not have models amenable to large-scale screening, have distinct dependency

profiles from tRCC despite sharing the same driver fusion. More broadly, many subtypes of kidney cancer apart from ccRCC have limited cellular or *in vivo* models and have been poorly characterized with respect to their molecular features and dependency landscapes.

In this study, we leveraged genome-scale CRISPR screening to discover selective vulnerabilities in tRCC cell line models. To complement this functional data, we applied a machine learning approach to nominate genetic dependencies based on tumor or cell line transcriptome profiles without the need for functional screening. By applying our predictive modeling to a broad range of tumor and cell line RNA-Seq datasets, with a focus on cancers not evaluated or underrepresented in prior functional screening efforts, we present a landscape of candidate vulnerabilities across multiple different *TFE3* fusion cancers, as well as across 13 different molecular subtypes of kidney cancer.

Results

Genome-scale CRISPR knockout screening of tRCC cells

We performed genome-scale pooled CRISPR-Cas9 knockout screening in three tRCC cell lines representing two distinct *TFE3* fusions (FUUR-1: *ASPSCR1-TFE3*; S-TFE: *ASPSCR1-TFE3*; UOK109: *NONO-TFE3*). Each cell line was stably transduced with Cas9 and subsequently transduced with a lentiviral library of 76,441 single-guide RNAs (sgRNAs) targeting 19,114 genes (Broad Brunello library (40)) with 1,000 non-targeting control sgRNAs. Cells were cultured for 28 days, at which point genomic DNA was extracted and sgRNA abundance was compared to the starting pool; sgRNAs depleted from the pool at the conclusion relative to the start of the experiment were inferred to target tRCC-essential genes (**Fig.1A**).

While the Cancer Dependency Map (DepMap) has profiled >1100 cancer cell lines across 28 lineages via genome-scale genetic (RNAi/CRISPR) screening, tRCC cell lines have to date not been included in this effort (30,41). We therefore sought to calibrate our results against published results from the DepMap in order to identify candidate vulnerabilities that are selectively essential in tRCC relative to other cancer types. For each gene assayed in our screens, we calculated a Chronos score, which represents the relative essentiality of a gene accounting for various potential confounders, including sgRNA efficiency, copy number related bias, and heterogenous cutting events (**Methods**) (31); by the Chronos metric, cell-essential genes have a score of approximately -1 while non-essential genes have a score of approximately 0 (31). We compared Chronos scores for each gene in tRCC cells (averaged across the 3 tRCC cell lines screened in our study) to Chronos scores for these same genes in either clear-cell renal cell carcinoma (ccRCC) cell lines (averaged across 14 cell lines) or all cancer lineages (averaged across 1193 cell lines representing 28 lineages, ccRCC excluded) screened in the DepMap (**Fig.1B-C, Supplementary Table S1, Methods**).

Using established lists of essential and non-essential genes(42), we found that essential genes (reported in DepMap) had a mean Chronos score of –0.930 across tRCC cell lines screened in our study, while non-essential genes had a mean Chronos score of -0.026. Importantly, while cell lines in the DepMap effort were screened using the Avana CRISPR knockout sgRNA library (74,687 sgRNAs targeting ~18,560 genes) (40) and the tRCC cell lines in this study utilized the Brunello library, the strong concordance in the scores for both essential and non-essential genes suggests that informative comparisons can be made between our data and those generated via the DepMap effort, despite the use of different genome-scale sgRNA libraries and the screens being conducted over different durations (43).

Among the most selective dependencies in tRCC cells were *TFE3* and *ASPSCR1* (fusion partner of *TFE3* in two of three cell lines screened) (**Fig.1B-C**). *TFE3* fusions typically retain the C-terminal exons of *TFE3* and the N-terminal exons of the fusion partner (23,44). As the Brunello sgRNA library contains 4 sgRNAs per gene, distributed across the gene body, we next sought to determine the log fold-change of individual sgRNAs in each of our CRISPR knockout screens. We found that sgRNAs targeting C-terminal exons of *TFE3* retained within the oncogenic fusion (E, F, G) were strongly depleted in our screens while an sgRNA targeting exon 4

105 (not contained within the oncogenic fusion, H) was not. Similarly, sgRNAs targeting N-terminal exons of the
106 *ASPSCR1* or *NONO* fusion partners were strongly depleted in cell lines containing the *ASPSCR1-TFE3* (s-TFE,
107 FU-UR-1) or *NONO-TFE3* fusions (UOK109), respectively. However, depletion of *NONO* sgRNAs was not
108 observed in s-TFE or FU-UR-1 cells, nor was depletion of *ASPSCR1* sgRNAs observed in UOK109 cells (**Fig.1D**,
109 **Supplementary Fig. S1A)**. We conclude that *TFE3* scores as a strongly selective dependency in tRCC lines due
110 to CRISPR-mediated depletion of the oncogenic driver fusion.

111 To further validate these findings, we performed growth competition assays in tRCC or ccRCC cell
112 lines transduced with Cas9 and either a control sgRNA or an sgRNA targeting *TFE3* (C-terminal region). Strong
113 depletion of *TFE3* knockout cells was observed in all *TFE3*-fusion tRCC cell lines, but not in ccRCC cell lines
114 that express wild type TFE3 (786-O, Caki-1) (**Fig.1E, Supplementary Table S2**). Together, these results
115 indicate that the driver *TFE3* fusion represents the primary selective essentiality in tRCC and that wild type
116 *TFE3* is dispensable in non-fusion cancer cells.

117 **Selectively essential pathways in tRCC**

118 We next sought to discover pathways that might represent selective essentialities in tRCC, beyond the
119 fusion itself. We performed gene ontology enrichment (45) on dependencies selectively essential to tRCC cell
120 lines (defined as ΔChronos ≤ -0.5 between every screened tRCC cell line and either ccRCC cell lines or all
121 lineages in DepMap, **Methods, Supplementary Table S1**). Remarkably, pathways related to oxidative
122 phosphorylation and mitochondrial metabolism were strongly enriched amongst tRCC-selective
123 dependencies (**Fig.2A**, **Supplementary Fig. S1B-C**), and multiple members of biochemical complexes
124 involved in these processes scored as strong selective dependencies in tRCC cells (**Fig.2B-D**). These included:
125 **(1)** genes involved in the transcription and translation of mitochondrially-encoded genes (*POLRMT*:
126 mitochondrial RNA Polymerase that transcribes mitochondrial DNA (mtDNA); *MRPL48*: component of the
127 mitochondrial ribosome ("mitoribosome"); *ERAL1*: involved in mitochondrial rRNA assembly; *NARS2*:
128 mitochondrial asparaginyl tRNA synthetase); **(2)** genes encoding enzymes in the citric acid (TCA) cycle (*SDHA,*
129 *SDHB*); **(3)** genes encoding components of the mitochondrial ATP synthase and electron transport chain
130 (*ATP5F1A, ATP5F1D, ATP5F1E, ATP5ME, ATP5PD, CYCS*); **(4)** genes involved in the assembly or biogenesis of
131 iron-sulfur clusters, which are critical for Complex I, II and III activity within the electron transport chain
132 (46)(*FDX2, HSCB, ISCA1*) (**Fig.2B, E**). Consistent with this screening data, we functionally validated that
133 knockout of several of these genes (*ISCA1, SDHA*, *MRPL48, POLRMT*) selectively impairs the growth of tRCC
134 cells in assays for cell proliferation, cell viability, and clonogenic capacity (**Fig.2F**, **Supplementary Fig. S2A-**
135 **D)**. Altogether, these results strongly validate our recent finding that *TFE3* fusions rewire tRCCs toward
136 oxidative phosphorylation, as opposed to the highly glycolytic metabolism of other kidney cancers (47).

137 Kidney lineage-defining transcription factors (*PAX8*, *HNF1B*) were also strong dependencies in tRCC,
138 as they are in ccRCC **(Fig.1C, Supplementary Fig. S1D)**. PAX8 is a transcription factor in the paired box family
139 that is critical for kidney organogenesis and is broadly expressed in renal epithelial cells as well as in renal
140 parietal cells (48). HNF1B is a homeodomain-containing transcription factor that also plays an important role
141 in nephron development; mutations in this gene represent the most common monogenic cause of
142 developmental renal disease (49). Consistent with these genes being lineage dependencies, knockout of
143 *HNF1B* and *PAX8* was selectively essential to both tRCC and ccRCC cell lines, as previously reported in ccRCC
144 (50), but had no effect on cancer cell lines of other lineages (**Supplementary Fig. S2F-K**). Moreover,
145 dependency of both *PAX8* and *HNF1B* correlated strongly with their expression across the DepMap (*HNF1B*: ρ
146 = -0.42, *P*=1.2e-48; *PAX8*: ρ = -0.26, *P*=2.1e-18) and both genes were highly expressed in tRCC and adjacent
147 kidney-normal tissue, but not in other *TFE3*-driven malignancies (melanotic kidney tumors, PEComa, ASPS)
148 that may be of mesenchymal origin (**Supplementary Fig. S2F-G**). Thus, although tRCCs often display
149 mesenchymal features distinct from most ccRCCs (51), these results functionally suggest that the cancer is
150 of a renal epithelial origin. Three genes involved in mevalonate synthesis (*PMVK, MVK, MVD*) were also strong
151 dependencies in tRCC and had variable levels of dependency across ccRCC cell lines (**Fig.2B-C**,

152 **Supplementary Fig. S2E**); given prior reports of perturbed cholesterol biosynthesis in ccRCC, this may also
153 represent a form of lineage dependency that holds across various types of kidney cancer (52,53).

154 Finally, we uncovered additional strong dependencies that were shared in two of the three screened
155 tRCC cell lines, including cell cycle related genes (*CDK4*), genes involved in hypoxia-inducible factor (HIF)
156 signaling (*EGLN1, VHL*), and genes involved in the antioxidant response (*TXNL4B*, *COA5/6*, *CYC1*)
157 (**Supplementary Fig. S1C**). These represent additional candidate vulnerabilities that could prove
158 therapeutically tractable.

159 **Predicting dependencies in tRCC based on transcriptional profile**

160 The relatively small number of tRCC models available for screening coupled with a diversity in *TFE3*
161 fusion partners and in co-occurring genetic alterations raises the possibility that some strong dependencies
162 may hold only in a subset of tRCC cases. We therefore sought to infer the dependency landscape of a cell line
163 or tumor from its transcriptional profile – a principle that could be broadly applicable since there are many
164 more tumors profiled by RNA sequencing (RNA-Seq) than there are cell line models amenable to large-scale
165 screening, for both tRCC and many other rare cancers.

166 Although it has been suggested that expression profiles may be used to predict vulnerabilities, prior
167 attempts have been applied primarily to cell line models, have had variable performance in tumor samples
168 (53–56), and have not typically been applied with the granularity of cancer subtypes. We sought to establish a
169 machine-learning model to reliably nominate genetic dependencies from cell line models and tumor RNA-Seq
170 data, with a focus on identifying highly predictable dependencies in rare cancer types for which cell line
171 models are not readily available for functional screening. Our pipeline involves merging and normalization of
172 RNA-Seq data from a cell line model or tumor of interest together with reference data (DepMap cell line or
173 TCGA tumor RNA-seq) followed by use of a machine learning model to predict dependencies; we elected to
174 use solely transcriptome profiles for dependency prediction given prior data that expression features have
175 greater predictive power for vulnerabilities than genomic features (54), and to establish the foundation for a
176 streamlined workflow that could be clinically translated (**Fig.3A, Methods**).

177 We first assessed our method on the DepMap dataset; we applied 5-fold cross-validation during the
178 train-test cycle using RNA-Seq expression features from each cell line to calculate a predicted Chronos score
179 for each gene. We elected to limit our predictions to highly predictable gene dependencies (defined as $R \geq 0.4$
180 for predicted vs. experimentally observed Chronos score, averaged across the 5 evaluation folds). We found
181 performance to be maximized with a support vector regression (SVR)-based model (RBF kernel) utilizing the
182 5000 strongest correlated gene expression features for prediction of each dependency. These criteria enabled
183 prediction of dependency scores for 657 genes (hereafter termed predictable dependencies, "PD"). The model
184 was then retrained on the entirety of the DepMap and deployed (**Supplementary Fig. S3A-C, Supplementary**
185 **Table S3, Methods**).

186 We applied our model to calculate predicted dependency scores for PD genes in the three tRCC cell
187 lines for which we had obtained a ground truth via genome-scale CRISPR screening in this study (FU-UR-1, s-
188 TFE, UOK109, **Supplementary Table S4**). We observed a strong correlation between predicted and observed
189 Chronos scores amongst the 657 PD genes in all of these cell lines (FU-UR-1: R=0.71, *P*=4.2e-100; s-TFE:
190 R=0.68, *P*=1.6e-86; UOK109: R=0.62, *P*=3.1e-70) (**Fig.3B**). We also predicted dependency scores in a fourth
191 tRCC cell line (UOK146), on which we had been unable to obtain high-quality genome-scale CRISPR screening
192 data owing to technical limitations (**Fig.3C, Supplementary Table S4**).

193 We nominated selective dependencies in each of these four tRCC cell lines relative to cancer cell lines
194 screened in the DepMap by comparing predicted Chronos scores for PD genes in each cell line to
195 experimentally derived Chronos scores for the same genes in the DepMap. The lineage dependencies *HNF1B*
196 and *PAX8* were prominently identified as selective in all tRCC cell lines, consistent with our screening data in

197 s-TFE, UOK109, and FU-UR-1, above. Mitochondrial superoxide dismutase (*SOD2*), identified in our screen as
198 a dependency in all cell lines (**Supplementary Table S1**, **Fig.2B**), was also a predicted dependency in two of
199 three screened cell lines (s-TFE, FU-UR-1, and narrowly missed the cutoff in the third, UOK109). In addition,
200 two other cell lines were predicted to be selectively dependent on *MDM2* (UOK109, UOK146), the E3 ubiquitin
201 ligase that negatively regulates the p53 tumor suppressor (57). Furthermore, *NFE2L2* and *SLC33A1* (which is
202 synthetically essential with NRF2 activation (58)) were predicted to be a dependency in FU-UR-1 cells (**Fig.3C**).

203 We then applied our dependency prediction to tRCC tumors profiled by RNA-Seq in three independent
204 studies (27,28,59) and again compared predicted Chronos scores to experimentally derived Chronos scores
205 in the DepMap. Reassuringly, dependencies predicted in tRCC cell lines were generally also predicted to be
206 selective dependencies in a subset of tRCC tumors, highlighting the applicability of our pipeline across both
207 cell line models and primary tumor data, and suggesting that existing tRCC models faithfully recapitulate
208 dependencies that would be present in tRCC tumors (**Fig.3D, Supplementary Fig. S3D, Supplementary**
209 **Table S4, Methods**).

210 We sought to validate predicted *MDM2* dependency in a subset of tRCC cell lines and tumors, given
211 that multiple small molecules targeting MDM2 are currently being clinically evaluated for cancer indications
212 (57). Consistent with our predictions, *MDM2* knockout selectively impaired viability and clonogenic capacity
213 in UOK109 and UOK146 cells but not in the other two tRCC cell lines (**Fig.3e, Supplementary Fig. S4A**). This
214 effect was phenocopied by the small molecule MDM2 inhibitor, milademetan, which has shown activity in
215 Phase I clinical trials (60) (**Fig.3F**). To further investigate the reason for divergent responses to milademetan
216 across our four tRCC cell lines, we analyzed whole-exome sequencing data in these cell lines. We observed
217 *TP53* mutations in s-TFE and FU-UR-1 cells (**Supplementary Fig. S4B**), likely explaining the lack of response
218 to milademetan in these two cell lines. Notably, across 88 tRCC tumors from 3 distinct datasets, selective
219 *MDM2* dependency was predicted in most tumors (82/88 [93.2%] tumors with $\Delta\text{Chronos}_{(\text{Predicted-DepMap Mean})} \leq -$
220 0.20, **Supplementary Fig. S3D**). The higher predicted frequency of MDM2-sensitive tRCC tumors relative to
221 cell lines may reflect the selection for *TP53* inactivation upon prolonged cell culture *in vitro*; by contrast,
222 genomic studies have indicated that tRCC tumors are almost always *TP53* wild-type (23,61,62).

223 Finally, we applied our dependency prediction to 20 genes previously reported to be altered in tRCC,
224 even if they were not included in our list of 657 PD genes (23,44). This analysis predicted *KMT2D* to be
225 selectively essential in s-TFE cells relative to other tRCC cell lines (**Supplementary Fig. S4C**), which we
226 validated via arrayed CRISPR/Cas9 knockout **(Supplementary Fig. S4D-E)**. Interestingly, *KMT2D* loss has been
227 associated with metabolic rewiring toward glycolytic metabolism (63). We have recently shown tRCC cells to
228 be dependent on OXPHOS and s-TFE cells have a highly OXPHOS-driven metabolic program (47), which may
229 explain their heightened sensitivity to *KMT2D* knockout.

230 Altogether, these data indicate the ability to predict potentially actionable dependencies from
231 transcriptome profiles of both tRCC cell line models and tumor samples.

232 ***MCL1* dependency in alveolar soft part sarcoma**

233 *TFE3* fusions drive a spectrum of rare cancers apart from tRCC, including alveolar soft part sarcoma
234 (ASPS), some endothelial hemangioendotheliomas (EHE), and some perivascular epithelioid cell tumors
235 (PEComa) (64–66). While these cancers share *TFE3* driver fusions, they may differ in terms of the cell of origin
236 as well as in co-occurring genetic driver alterations. We therefore sought to determine whether the
237 dependency profile of ASPS differs from that of tRCC. We performed RNA-seq on two ASPS cell lines: ASPS-1
238 and ASPS-KY, both of which were too slow-growing to be amenable to genome-scale CRISPR screening, and
239 used our method to predict selective dependencies in ASPS relative to tRCC (**Fig.4A-B, Supplementary Table**
240 **S4**). Similar predictions were performed on published RNA-Seq data from seven ASPS tumors (67). Although
241 the dependency profiles of tRCC and ASPS cell lines were largely concordant (R=0.64), several dependencies
242 were predicted to be selective for ASPS cells versus tRCC, including *MCL1* and *PRKRA*. Conversely, and

243 consistent with tRCCs being of renal epithelial origin and ASPS being of a mesenchymal origin, the renal
244 lineage dependencies *PAX8* and *HNF1B* were not predicted in ASPS (**Fig.4A-C**, **Supplementary Fig. S3D**).

245 We also predicted dependencies in PEComa and EHE, two other sarcomas that can be driven by *TFE3*
246 fusions (64,68) and identified vulnerabilities in PD genes that were selective for these malignancies relative to
247 the cell lines experimentally screened in the DepMap, using the procedure described above. Most selective
248 dependencies predicted in these two rare cancers were shared with ASPS (e.g. *FGFR1*, *MCL1*, *PRKAR1A*,
249 *PRKRA*), including the well validated mesenchymal dependency: *GPX4* (69), consistent with all three tumors
250 being sarcomas (**Fig.4C, Supplementary Fig. S5A-C, Supplementary Table S4**).

251 Targeting of *MCL1* or *PRKRA* by three distinct sgRNAs selectively impaired viability in ASPS cells (ASPS-
252 1 and ASPS-KY) relative to tRCC cells (UOK109, FUUR-1, S-TFE) (**Fig.4D**, **Supplementary Fig. S5D-F**). Similar
253 profiles of differential sensitivity were observed using the clinical-grade MCL1 inhibitor murizatoclax (70)
254 (**Fig.4E**). To gain additional insights into predictors of *MCL1* sensitivity, we identified features predicting *MCL1*
255 dependency in our model across DepMap cell lines; the top predictor was low *BCL2L1* expression (**Fig.4F**).
256 *BCL2L1* encodes the anti-apoptotic factor BCL-xL, which has itself been identified as a dependency in a subset
257 of ccRCC (71). Lower *BCL2L1* expression strongly correlated with greater *MCL1* dependency (ρ=0.50, P=8.2e-
258 71, **Fig.4G**). We further analyzed *BCL2L1* expression in ASPS cell lines/tumors versus tRCC cell lines/tumors
259 and kidney cancer-adjacent normal tissue, when available, and observed substantially lower *BCL2L1*
260 expression in ASPS relative to tRCC and kidney-adjacent normal tissue (**Fig.4H**).

261 Overall, these analyses highlight the fact that tRCC and ASPS harbor distinct selective vulnerabilities,
262 despite both cancers sharing the same driver fusion; these differences may be linked to a different cell of origin
263 in each tumor.

264 **Predicting dependencies and therapeutic response across cancer types**

265 We next sought to validate our approach across diverse cancer types. We applied our model to predict
266 dependency scores for PD genes for 11,373 tumors representing 33 lineages in The Cancer Genome Atlas
267 (TCGA) (**Supplementary Table S4**). Reassuringly, when clustered (t-distributed Stochastic Neighbor
268 Embedding, t-SNE) on the basis of predicted dependency score, TCGA tumors clustered by lineage together
269 with cell lines experimentally screened in the DepMap (**Supplementary Fig. S6A**). Dependency prediction in
270 the TCGA recovered strong predicted lineage dependencies in the expected patterns, including *SOX10* in
271 melanoma (both cutaneous and uveal) (72,73) and *CTNNB1* in colorectal cancers (74–76) (**Fig.5A)**. Although
272 our model predicts dependency scores based on the top 5000 expression features, relative feature weights
273 may vary widely from gene to gene. In the case of *SOX10* predicted dependency, *SOX10* expression was
274 weighted most heavily, with *CDH19* feature weight being comparable. Notably, *CDH19* is a direct
275 transcriptional target of SOX10 and plays a critical role in neural crest cell development and migration (77). In
276 the case of *CTNNB1*, multiple biologically plausible expression features were linked to β-catenin signaling
277 predicted dependency, including *AXIN2*, *NKD1*, *ASCL2*, and *BMP4* (78–80) (**Fig.5B**). Our modeling also
278 predicted *CDK4* dependency in a subset of cancers across diverse lineages, notably including breast cancer,
279 where CDK4/6 inhibitors are approved but reliable single-gene biomarkers have proven elusive (81). Finally,
280 dependency on glutathione peroxidase 4 (*GPX4*) was predicted to be most pronounced in mesenchymal
281 lineages, consistent with prior studies (69) (**Fig.5A-B**). We conclude that our approach can recover
282 dependencies predicted by outlier expression of one or two genes (e.g. many lineage dependencies) as well as
283 those correlated with more complex expression profiles.

284 We next sought to infer the dependency profiles of cell line models that have not yet been subjected
285 to unbiased genetic screening. We predicted dependencies in 458 cell lines that were molecularly
286 characterized in the Cancer Cell Line Encyclopedia (CCLE) effort but which have not yet been subjected to
287 genome-scale CRISPR screening in the DepMap (82) **(Supplementary Table S4)**. A subset of these cell lines
288 (restricting to solid tumor lineages with ≥10 cell lines; N=251) were then clustered on the basis of their

289 predicted dependency profile, together with 833 cell lines experimentally screened in the DepMap (using
290 experimentally-derived dependency scores for the latter lines). Reassuringly, cell lines and tumors with
291 predicted dependency profiles clustered primarily with experimentally screened cell lines of the same lineage
292 (**Fig.5C**, **Supplementary Fig. S6A**). However, there were notable and informative exceptions. For example, one
293 cell line of mucinous ovarian origin (JHOM2B) clustered together with screened cell lines of bowel lineage; this
294 was driven by shared dependencies on Wnt pathway members (*CTNNB1*, *TCF7L2*) (74), the Wnt-regulated
295 colon lineage-defining transcription factor *SOX9* (83), and *KRAS* (76) (**Supplementary Fig. S6B**). Notably,
296 treatment of mucinous ovarian cancer with gastrointestinal-type chemotherapy regimens is preferred and
297 associated with better outcomes compared to gynecologic regimens (84). Kidney cancer cell lines also
298 clustered in distinct groups. While a majority of screened and predicted cell lines of kidney origin clustered
299 together (**Fig.5c**), five kidney cancer cell lines, whose dependency scores were predicted, clustered together
300 with screened rhabdoid-like cell lines from distinct lineages (malignant rhabdoid tumors of the kidney,
301 extrarenal rhabdoid tumors, embryonal rhabdomyosarcoma, atypical teratoid/rhabdoid tumors (ATRT), and
302 small cell ovarian cancers (ovarian rhabdoid tumors)) (**Fig.5C**). This co-clustering was driven by shared
303 dependencies on polycomb repressive complex 2 (PRC2) subunits (*EZH2*, *EED*) (85–89) and transcriptional
304 activator *EP300* (90) (**Supplementary Fig. S6C-D**). This implies that a tumor's dependency profile can vary
305 considerably based on histologic subtype and other factors and may not merely reflect the organ from which
306 it is derived.

307 Finally, we explored whether our model could inform response to therapeutic agents with defined
308 molecular targets. While drugs targeting the mammalian target of rapamycin (mTOR) pathway are approved
309 and frequently employed in kidney cancer, accurate biomarkers for patient selection have proven elusive (91).
310 Although *MTOR* was not included in the list of 657 PD genes, it was predicted with reasonable accuracy during
311 testing (R = 0.32, averaged from 5-fold cross-validation). We predicted *MTOR* dependency using tumor RNA-
312 Seq data from patients enrolled in the Checkmate 025 study, a Phase 3 study that compared nivolumab
313 (immune checkpoint inhibitor) with everolimus (mTOR inhibitor) in patients with clear cell renal-cell carcinoma
314 (92). Stratifying by predicted *MTOR* dependency score (median dichotomized), high predicted *MTOR*
315 dependency correlated with better overall (P=0.0078) and progression-free survival (P=0.0381) on the
316 everolimus arm but not the nivolumab arm (OS: P=0.0671, PFS: P=0.9641). Moreover, patients in the
317 everolimus arm with high predicted *MTOR* dependency had similar outcomes to those treated with nivolumab
318 (OS: P=0.3575, PFS: P=0.5949), although nivolumab was superior to everolimus in the overall unselected
319 population (OS: P=0.0069, PFS: P=0.0846) (**Fig.5D**, **Supplementary Fig. S6E)**. Dichotomization by predicted
320 *MTOR* dependency score predicted overall survival on the everolimus arm better than dichotomization using
321 any of the other 657 PD genes (**Supplementary Fig. S6F**). *MTOR* dependency prediction was driven by multiple
322 expression features, with the top predictive feature in DepMap (*DENND2D* expression) also being highly ranked
323 in our model (rank 80/5000) (**Supplementary Fig. S6G**).

324 Together, these results suggest that our approach can be used to both nominate dependencies and
325 inform response to molecularly-targeted therapies across a wide array of tumor types.

326 **A candidate dependency landscape across rare kidney cancers**

327 Having established the tractability of our approach for nominating dependencies across diverse
328 cancer types, we turned our attention to defining the landscape of dependencies across kidney cancers, which
329 comprise a notoriously heterogeneous group of > 40 molecularly distinct subtypes in both adults and children
330 (13). Many of these cancer types have been poorly characterized, are lacking in cell line models amenable to
331 high throughput screening and represent unmet medical needs. We reasoned that dependency prediction
332 could be used to nominate selective dependencies in several of these molecularly-defined entities, in order to
333 better define the spectrum of dependencies across kidney cancer subtypes.

By surveying published studies, we collected RNA-Seq data of 851 tumors across 13 kidney cancer subtypes and used these data to calculate predicted dependency scores for 657 PD genes, as above (**Fig.6A, Supplementary Table S4**). These tumors were then clustered based on dependency profile together with 22 renal cancer cell lines from the DepMap (on which dependency scores were experimentally determined). Group 1 was comprised primarily of ccRCC tumors and most RCC cell lines (which are enriched for clear-cell type (93)), as well as metabolically divergent chRCC (MD-chRCC) tumors. MD-chRCC have been previously described as a distinct, clinically aggressive subset of chRCC with a distinctive hypermethylation pattern and lacking chromosomal losses normally associated with classical chRCC (59). Interestingly, most MD-chRCC tumors demonstrate sarcomatoid differentiation, which may also be seen in a subset of ccRCC tumors (59,94). Group 2 comprised papillary RCC (pRCC type 1 and type 2) as well as a number of diverse entities that have been historically classified as papillary type 2 RCC (95), including CpG island methylator phenotype RCC (CIMP-RCC) and fumarate hydratase (FH)-deficient RCC. Finally, Group 3 consisted of oncocytic tumors, including chRCC and eosinophilic chRCC (**Fig.6B**, **Supplementary Fig. S6H**). Thus, in total, this analysis collapsed 13 distinct subtypes of RCC into three main dependency classes.

We then more carefully interrogated potentially actionable subtype-specific dependencies in kidney cancer. We performed hierarchical clustering of dependency profiles, restricting to 17 genes selective to at least one of the three dependency groups, and including an additional 46 genes with known drug targets. Clustering based on predicted dependency score recapitulated the broad structure observed on t-SNE based clustering above and lent additional insight into specific pairwise comparisons between subtypes (**Fig.6C**). For example, the lineage transcription factors *HNF1B* and *PAX8* were predicted to be very strong dependencies in ccRCC, papillary type 1 and type 2, and most other RCC subtypes with the notable exception of the oncocytic tumors (chRCC, eosinophilic chRCC, oncoytoma, and MD chRCC); this is likely consistent with the former classes of tumors arising from proximal tubule kidney epithelial cells and the latter class arising from mitochondria-rich cells of the distal nephron (96). Notably, *PAX8* and *HNF1B* vary in expression level throughout the nephron, and these gene dependencies are highly correlated to expression level (97,98). Moreover, *HNF1B* is essential for the development of the proximal but not distal tubule(99) (**Fig.6D**, **Supplementary Fig. S2**).

We also observed differential *KEAP1* and *NFE2L2* dependency across RCC subtypes (**Fig.6E**). In particular, FH-deficient RCC and CIMP-RCC were predicted to be strongly dependent on *NFE2L2*, consistent with prior reports of NRF2 pathway activation in these subtypes via methylation of *KEAP1* (CIMP-RCC) or succinylation of *KEAP1* (FH-RCC) (100–102). Although *KEAP1* loss activates NRF2, which is typically oncogenic (103), a subset of RCCs across lineages had predicted dependency scores suggestive of *KEAP1* dependency. This is consistent with recent studies demonstrating that cancers may be sensitive to both oxidative stress (*NFE2L2* dependency) and reductive stress (*KEAP1* dependency), depending on their underlying metabolic features (47,104,105).

Other dependencies appeared to reflect differing rates of genomic alterations across RCC subtypes. For example, *DDX3X* dependency, a paralog dependency known to be unmasked by loss of the Y-chromosome encoded paralog *DDX3Y* (106), was predicted to be among the strongest in pRCC-T1, a tumor type with almost universal somatic loss of the Y chromosome (LOY) (107); accordingly, *DDX3X* dependency was nearly identical between male and female pRCC-T1 samples, but male ccRCC samples (which typically do not show LOY) were far less dependent on *DDX3X,* due to paralog buffering from *DDX3Y* (**Fig.6F**). Most kidney tumors were expected to be dependent on *MDM2*, consistent with the low frequency of *TP53* mutations in this lineage (108); however, *TP53* mutant tumors were predicted to be less *MDM2* dependent than their lineage-matched *TP53* wild-type counterparts (**Supplementary Fig. S6I**).

Dependencies in selenium metabolism (*SEPHS2, SEPSECS, GPX4*), which would be predicted to induce cell death via ferroptosis, were strongest in ccRCC, consistent with prior functional studies in this

380 subtype (109). MD-chRCC also shared this profile, consistent with most MD-chRCCs displaying a
381 mesenchymal signature associated with ferroptosis sensitivity (59,69). Other RCC subtypes also differed in
382 their predicted dependency on various genes involved in apoptotic cell death (*BCL2*, *MCL1*, *BCL2L1*), with FH-
383 deficient RCC and CIMP-RCC predicted to be particularly dependent on *BCL2L1* and oncocytic tumors more
384 dependent on *BCL2*. By contrast to ASPS, as discussed above, few RCCs showed predicted dependency on
385 *MCL1* (**Fig.6G**). Overall, these analyses suggest subtype differences in vulnerabilities to specific modes of cell
386 death.

387 Finally, we sought to nominate dependencies in renal tumors with sarcomatoid and/or rhabdoid
388 differentiation (S/R RCCs) (**Supplementary Table S4**); these aggressive features are thought to represent a
389 dedifferentiation event that can occur in renal tumors of diverse parental histologies (94). Despite being
390 clinically aggressive, immune checkpoint inhibitors appear to be particularly effective in S/R RCC for
391 somewhat unclear reasons and additional treatment strategies for this subset of RCC represent an unmet
392 need (94). Using previously annotated S/R RCCs within the TCGA (94), we identified predicted dependencies
393 that were selective to S/R RCCs. Dependencies related to PRMT5 function (*MAT2A* (99) and *WDR77*) were
394 prominently identified as S/R RCC-selective. These likely stem from the established synthetic lethal
395 relationship of *PRMT5* and *MTAP* deletion (110,111); *MTAP* is frequently co-deleted with *CDKN2A,* a deletion
396 event that is strongly enriched in S/R RCCs (23). Additional S/R RCC-selective dependencies include *PPP2CA*,
397 the gene encoding protein phosphatase-PP2A. Notably, PP2A inhibitors have been clinically developed and
398 shown durable anti-tumor activity when combined with immune checkpoint blockade (112,113). Finally,
399 *BCL2L1* dependency is also predicted to be enriched in S/R RCC. *BCL2L1*, which encodes the BCL-xL
400 antiapoptotic protein, has recently been reported as a dependency of mesenchymal kidney cancers;
401 intriguingly, S/R RCCs are known to strongly upregulate epithelial-mesenchymal transition (EMT) programs
402 (**Fig.6H**) (71,94).

403 Notably, S/R RCCs were derived from all RCC groups, with the majority being derived from group 1
404 (comprised of ccRCCs and MD-chRCCs) (**Fig.6GG**, **Supplementary Fig. S6J**). This analysis supports the ability
405 to recover candidate dependencies associated with the sarcomatoid differentiation state, rather than only
406 those linked to the lineage from which S/R RCCs are derived. This also suggests that kidney cancers of various
407 histologies may converge on a dependency profile associated with this sarcomatoid/mesenchymal state.

408 Overall, we provide a landscape of dependencies in rare kidney cancers that could be used as a
409 starting point to develop mechanism-inspired therapeutic strategies in these diseases.

410 Discussion

411 In this study, we performed genome-scale CRISPR knockout screening in three cell line models of
412 tRCC, a rare renal tumor not previously included in large scale screening efforts. We identify the *TFE3* fusion
413 as the primary vulnerability in tRCC, consistent with recent genomic studies demonstrating that the fusion
414 represents the dominant, and often sole, driver event in this cancer (23,25–28,44). Given the dispensability *of*
415 *TFE3* in normal tissues (114) and in all cancer cell lines screened to date in the DepMap, the *TFE3* fusion
416 represents an attractive and highly selective target in tRCC, albeit challenging from the standpoint of
417 druggability.

418 Our study also reveals additional selective vulnerabilities in tRCC, most notably multiple genes
419 involved in mitochondrial metabolism and oxidative phosphorylation, including components of the citric acid
420 (TCA) cycle, mitochondrial transcription and translation, and the electron transport chain. These unbiased
421 screens dovetail remarkably with our recent study demonstrating that TFE3 fusions metabolically rewire
422 tRCCs towards oxidative phosphorylation (OXPHOS) via transcriptional activation of multiple genes involved
423 in oxidative metabolism and mitochondrial biogenesis (47). They are also consistent with the role of wild type
424 TFE proteins as critical regulators of energy metabolism (115–117). Individual genes within these or related

425 pathways may represent more tractable therapeutic targets than the fusion itself and may represent inroads
426 to modulate critical downstream pathways driven by TFE3.

427 However, our tRCC screens also highlight a critical limitation of unbiased functional genomics in rare
428 cancers - namely, the number and availability of suitable models. Over fifteen different *TFE3* fusion partners
429 have been reported (23), but only two distinct fusions were represented in the three cell lines screened in this
430 study. For example, we found the tRCC cell line UOK146, which harbors the relatively common *PRCC-TFE3*
431 fusion (23), to be not technically amenable to genome-scale CRISPR knockout screening. Additionally, while
432 ASPS is also driven by a TFE3-fusion, available ASPS cell lines are slow growing and challenging to culture at
433 the scale required for genome-scale screening. Many other rare adult and pediatric malignancies that would
434 benefit from targeted therapeutics have not been included in unbiased functional screening efforts due to their
435 rarity or due to existing models being unamenable to screening.

436 We attempted to bridge this gap by pursuing the alternative approach of predicting a tumor's
437 dependency landscape via its transcriptional profile. Recent studies have reported approaches to predict a
438 tumor's dependency profile by virtue of its transcriptional and/or genomic features (54,56,118). While each of
439 these models differs somewhat in approach, all are complementary and formal benchmarking would be
440 required to hone the most accurate method for predicting tumor vulnerabilities. Our approach utilizes
441 predictive expression features that can be readily obtained by clinical transcriptome sequencing of tumor
442 tissue and we suggest that this or a similar approach can be broadly useful to guide treatment selection in rare
443 cancers, for which there is often no evidence-based standard of care. This approach may also be developed
444 to therapies that have a clearly defined molecular target (e.g. everolimus) but no robust biomarker in clinical
445 use.

446 We predict and validate dependencies across a host of rare cancer types not well-represented in the
447 TCGA and validate several key examples. Via this approach we identified differential dependencies between
448 tRCC and ASPS despite both cancers sharing the same driver fusion, with ASPS cells being selectively sensitive
449 to MCL1 inhibition. Notably, multiple MCL1 inhibitors have advanced clinically; although cardiac toxicity has
450 proven a challenge to earlier agents, newer MCL1 inhibitors appear not to have this liability (119,120). Our
451 study suggests that CDK4/6 inhibitors, EGLN1 inhibitors (47), and MDM2 inhibitors represent additional
452 classes of agents with clinically advanced molecules that could be tested for activity in tRCC or ASPS.

453 Finally, by applying dependency prediction to a spectrum of kidney cancers, we suggest that kidney
454 cancer subtypes have notably distinct dependency landscapes. Remarkably, although there are several dozen
455 histologic types of kidney cancer, many with multiple expression subtypes (13), we find that kidney cancers
456 collapse into three main groups in dependency space. Intriguingly, S/R RCCs (which can be derived from
457 various RCC subtypes) span multiple dependency clusters and share a small set of unique dependencies.
458 Most discovery biology in kidney cancer has to date has focused on ccRCC: while this has resulted in marked
459 improvements in the treatment of ccRCC over the last decade, these therapies are typically less effective in
460 non-ccRCCs (121), which may be driven by distinct biology. Dependencies related to energy metabolism
461 encapsulate this notion: while deficiency in TCA cycle enzymes such as FH and SDHA/B drives tumorigenesis
462 in glycolytic renal cancers (e.g. FH-RCC and ccRCC), these same genes represent dependencies in high
463 OXPHOS renal cancers such as tRCC (47). We nominate several potentially actionable dependencies,
464 including BCL-xL (*BCL2L1*), *DDX3X*, *MAT2A* and *NFE2L2* that may represent novel therapeutic targets in
465 subsets of kidney cancer.

466 Overall, we suggest that our combined approach of functional screening and dependency prediction
467 may catalyze precision oncology in many settings, particularly for rare cancers and in many pediatric cancers,
468 where experimental models may be limited, or where discovery biology efforts are resource-limited by small
469 commercial markets and modest industry investment.

References

1. Konda P, Garinet S, Van Allen EM, Viswanathan SR. Genome-guided discovery of cancer therapeutic targets. Cell Reports. 2023;42:112978.

2. Hahn WC, Bader JS, Braun TP, Califano A, Clemons PA, Druker BJ, et al. An expanded universe of cancer targets. Cell. 2021;184:1142–55.

3. Garraway LA, Lander ES. Lessons from the Cancer Genome. Cell. 2013;153:17–37.

4. MacConaill LE, Garraway LA. Clinical Implications of the Cancer Genome. JCO. Wolters Kluwer; 2010;28:5219–28.

5. Basu A, Bodycombe NE, Cheah JH, Price EV, Liu K, Schaefer GI, et al. An interactive resource to identify cancer genetic and lineage dependencies targeted by small molecules. Cell. 2013;154:1151–61.

6. Parrish PCR, Thomas JD, Gabel AM, Kamlapurkar S, Bradley RK, Berger AH. Discovery of synthetic lethal and tumor suppressor paralog pairs in the human genome. Cell Reports. 2021;36:109597.

7. Behan FM, Iorio F, Picco G, Gonçalves E, Beaver CM, Migliardi G, et al. Prioritization of cancer therapeutic targets using CRISPR–Cas9 screens. Nature. 2019;568:511–6.

8. Pacini C, Duncan E, Gonçalves E, Gilbert J, Bhosle S, Horswell S, et al. A comprehensive clinically informed map of dependencies in cancer cells and framework for target prioritization. Cancer Cell. Elsevier; 2024;42:301-316.e9.

9. Viswanathan SR, Nogueira MF, Buss CG, Krill-Burger JM, Wawer MJ, Malolepsza E, et al. Genome-scale analysis identifies paralog lethality as a vulnerability of chromosome 1p loss in cancer. Nat Genet. 2018;50:937–43.

10. Jamshidi F, Nielsen TO, Huntsman DG. Cancer genomics: why rare is valuable. J Mol Med. 2015;93:369–81.

11. Dharia NV, Kugener G, Guenther LM, Malone CF, Durbin AD, Hong AL, et al. A first-generation pediatric cancer dependency map. Nat Genet. Nature Publishing Group; 2021;53:529–38.

12. Sharifnia T, Wawer MJ, Goodale A, Lee Y, Kazachkova M, Dempster JM, et al. Mapping the landscape of genetic dependencies in chordoma. Nat Commun. 2023;14:1933.

13. Moch H, Cubilla AL, Humphrey PA, Reuter VE, Ulbright TM. The 2016 WHO Classification of Tumours of the Urinary System and Male Genital Organs—Part A: Renal, Penile, and Testicular Tumours. European Urology. 2016;70:93–105.

14. Schödel J, Grampp S, Maher ER, Moch H, Ratcliffe PJ, Russo P, et al. Hypoxia, Hypoxia-inducible Transcription Factors, and Renal Cancer. European Urology. 2016;69:646–57.

504 15. Shirole NH, Kaelin WG. von-Hippel Lindau and Hypoxia-Inducible Factor at the Center of
505 Renal Cell Carcinoma Biology. Hematol Oncol Clin North Am. 2023;37:809–25.

506 16. John A, Spain L, Hamid AA. Navigating the Current Landscape of Non-Clear Cell Renal Cell
507 Carcinoma: A Review of the Literature. Current Oncology. Multidisciplinary Digital Publishing
508 Institute; 2023;30:923–37.

509 17. Kauffman EC, Ricketts CJ, Rais-Bahrami S, Yang Y, Merino MJ, Bottaro DP, et al. Molecular
510 genetics and cellular features of TFE3 and TFEB fusion kidney cancers. Nat Rev Urol.
511 2014;11:465–75.

512 18. Choueiri TK, Lim ZD, Hirsch MS, Tamboli P, Jonasch E, McDermott DF, et al. Vascular
513 endothelial growth factor-targeted therapy for the treatment of adult metastatic Xp11.2
514 translocation renal cell carcinoma. Cancer. 2010;116:5219–25.

515 19. Malouf GG, Camparo P, Oudard S, Schleiermacher G, Theodore C, Rustine A, et al. Targeted
516 agents in metastatic Xp11 translocation/TFE3 gene fusion renal cell carcinoma (RCC): a
517 report from the Juvenile RCC Network. Ann Oncol. 2010;21:1834–8.

518 20. Boilève A, Carlo MI, Barthélémy P, Oudard S, Borchiellini D, Voss MH, et al. Immune
519 checkpoint inhibitors in MITF family translocation renal cell carcinomas and genetic
520 correlates of exceptional responders. j immunotherapy cancer. 2018;6:159.

521 21. Chanzá NM, Xie W, Bilen MA, Dzimitrowicz H, Burkart J, Geynisman DM, et al. Cabozantinib
522 in advanced non-clear-cell renal cell carcinoma: a multicentre, retrospective, cohort study.
523 Lancet Oncol. 2019;20:581–90.

524 22. Alhalabi O, Thouvenin J, Négrier S, Vano Y-A, Campedel L, Hasanov E, et al. Immune
525 Checkpoint Therapy Combinations in Adult Advanced MiT Family Translocation Renal Cell
526 Carcinomas. The Oncologist. 2023;28:433–9.

527 23. Bakouny Z, Sadagopan A, Ravi P, Metaferia NY, Li J, AbuHammad S, et al. Integrative clinical
528 and molecular characterization of translocation renal cell carcinoma. Cell Rep.
529 2022;38:110190.

530 24. Malouf GG, Monzon FA, Couturier J, Molinié V, Escudier B, Camparo P, et al. Genomic
531 heterogeneity of translocation renal cell carcinoma. Clin Cancer Res. 2013;19:4673–84.

532 25. Malouf GG, Su X, Yao H, Gao J, Xiong L, He Q, et al. Next-generation sequencing of
533 translocation renal cell carcinoma reveals novel RNA splicing partners and frequent
534 mutations of chromatin-remodeling genes. Clin Cancer Res. 2014;20:4129–40.

535 26. Marcon J, DiNatale RG, Sanchez A, Kotecha RR, Gupta S, Kuo F, et al. Comprehensive
536 Genomic Analysis of Translocation Renal Cell Carcinoma Reveals Copy-Number Variations
537 as Drivers of Disease Progression. Clin Cancer Res. 2020;26:3629–40.

538 27. Sun G, Chen J, Liang J, Yin X, Zhang M, Yao J, et al. Integrated exome and RNA sequencing of
539 TFE3-translocation renal cell carcinoma. Nat Commun. Nature Publishing Group;
540 2021;12:5262.

541 28. Qu Y, Wu X, Anwaier A, Feng J, Xu W, Pei X, et al. Proteogenomic characterization of MiT
542 family translocation renal cell carcinoma. Nat Commun. Nature Publishing Group;
543 2022;13:7494.

544 29. Meyers RM, Bryan JG, McFarland JM, Weir BA, Sizemore AE, Xu H, et al. Computational
545 correction of copy number effect improves specificity of CRISPR-Cas9 essentiality screens
546 in cancer cells. Nat Genet. 2017;49:1779–84.

547 30. Tsherniak A, Vazquez F, Montgomery PG, Weir BA, Kryukov G, Cowley GS, et al. Defining a
548 Cancer Dependency Map. Cell. 2017;170:564-576.e16.

549 31. Dempster JM, Boyle I, Vazquez F, Root DE, Boehm JS, Hahn WC, et al. Chronos: a cell
550 population dynamics model of CRISPR experiments that improves inference of gene fitness
551 effects. Genome Biol. 2021;22:343.

552 32. Ishiguro M, Iwasaki H, Ohjimi Y, Kaneko Y. Establishment and characterization of a renal cell
553 carcinoma cell line (FU-UR-1) with the reciprocal ASPL-TFE3 fusion transcript. Oncol Rep.
554 2004;11:1169–75.

555 33. Hirobe M, Masumori N, Tanaka T, Kitamura H, Tsukamoto T. Establishment of an ASPL-TFE3
556 renal cell carcinoma cell line (S-TFE). Cancer Biol Ther. 2013;14:502–10.

557 34. Calandrini C, Schutgens F, Oka R, Margaritis T, Candelli T, Mathijsen L, et al. An organoid
558 biobank for childhood kidney cancers that captures disease and tissue heterogeneity. Nat
559 Commun. 2020;11:1310.

560 35. Fujiwara T, Kunisada T, Nakata E, Nishida K, Yanai H, Nakamura T, et al. Advances in
561 treatment of alveolar soft part sarcoma: an updated review. Jpn J Clin Oncol. 2023;53:1009–
562 18.

563 36. Argani P, Gross JM, Baraban E, Rooper LM, Chen S, Lin M-T, et al. TFE3 -Rearranged
564 PEComa/PEComa-like Neoplasms : Report of 25 New Cases Expanding the
565 Clinicopathologic Spectrum and Highlighting its Association With Prior Exposure to
566 Chemotherapy. Am J Surg Pathol. 2024;48:777–89.

567 37. Neil E, Kouskoff V. Current Model Systems for Investigating Epithelioid
568 Haemangioendothelioma. Cancers (Basel). 2023;15:3005.

569 38. Panagopoulos I, Gorunova L, Lund-Iversen M, Bassarova A, Heim S. Fusion of the Genes
570 PHF1 and TFE3 in Malignant Chondroid Syringoma. Cancer Genomics Proteomics.
571 2019;16:345–51.

572 39. Suurmeijer AJH, Song W, Sung Y-S, Zhang L, Swanson D, Fletcher CDM, et al. Novel
573 recurrent PHF1-TFE3 fusions in ossifying fibromyxoid tumors. Genes Chromosomes Cancer.
574 2019;58:643–9.

575 40. Doench JG, Fusi N, Sullender M, Hegde M, Vaimberg EW, Donovan KF, et al. Optimized
576 sgRNA design to maximize activity and minimize off-target effects of CRISPR-Cas9. Nat
577 Biotechnol. 2016;34:184–91.

41. DepMap, Broad (2024). Current DepMap Release data, including CRISPR Screens, PRISM Drug Screens, Copy Number, Mutation, Expression, and Fusions. DepMap 23Q2 Public. Figshare+. Dataset.;

42. Hart T, Chandrashekhar M, Aregger M, Steinhart Z, Brown KR, MacLeod G, et al. High-Resolution CRISPR Screens Reveal Fitness Genes and Genotype-Specific Cancer Liabilities. Cell. 2015;163:1515–26.

43. Dempster JM, Pacini C, Pantel S, Behan FM, Green T, Krill-Burger J, et al. Agreement between two large pan-cancer CRISPR-Cas9 gene dependency data sets. Nat Commun. 2019;10:5817.

44. Achom M, Sadagopan A, Bao C, McBride F, Xu Q, Konda P, et al. A genetic basis for cancer sex differences revealed in Xp11 translocation renal cell carcinoma [Internet]. bioRxiv; 2023 [cited 2023 Aug 9]. page 2023.08.04.552029. Available from: https://www.biorxiv.org/content/10.1101/2023.08.04.552029v1

45. Kuleshov MV, Jones MR, Rouillard AD, Fernandez NF, Duan Q, Wang Z, et al. Enrichr: a comprehensive gene set enrichment analysis web server 2016 update. Nucleic Acids Res. 2016;44:W90-97.

46. Read AD, Bentley RE, Archer SL, Dunham-Snary KJ. Mitochondrial iron-sulfur clusters: Structure, function, and an emerging role in vascular biology. Redox Biol. 2021;47:102164.

47. Li J, Huang K, McBride F, Sadagopan A, Gallant DS, Thakur M, et al. TFE3 fusions direct an oncogenic transcriptional program that drives OXPHOS and unveils vulnerabilities in translocation renal cell carcinoma [Internet]. bioRxiv; 2024 [cited 2024 Aug 10]. page 2024.08.09.607311. Available from: https://www.biorxiv.org/content/10.1101/2024.08.09.607311v1

48. Tong G-X, Yu WM, Beaubier NT, Weeden EM, Hamele-Bena D, Mansukhani MM, et al. Expression of PAX8 in normal and neoplastic renal tissues: an immunohistochemical study. Modern Pathology. 2009;22:1218–27.

49. Clissold RL, Hamilton AJ, Hattersley AT, Ellard S, Bingham C. HNF1B-associated renal and extra-renal disease—an expanding clinical spectrum. Nat Rev Nephrol. 2015;11:102–12.

50. Patel SA, Hirosue S, Rodrigues P, Vojtasova E, Richardson EK, Ge J, et al. The renal lineage factor PAX8 controls oncogenic signalling in kidney cancer. Nature. 2022;606:999–1006.

51. Prakasam G, Mishra A, Christie A, Miyata J, Carrillo D, Tcheuyap VT, et al. Comparative genomics incorporating translocation renal cell carcinoma mouse model reveals molecular mechanisms of tumorigenesis. J Clin Invest. 2024;134:e170559.

52. Riscal R, Bull CJ, Mesaros C, Finan JM, Carens M, Ho ES, et al. Cholesterol Auxotrophy as a Targetable Vulnerability in Clear Cell Renal Cell Carcinoma. Cancer Discovery. 2021;11:3106–25.

614 53. Thompson JM, Alvarez A, Singha MK, Pavesic MW, Nguyen QH, Nelson LJ, et al. Targeting the
615 Mevalonate Pathway Suppresses VHL-Deficient CC-RCC through an HIF-Dependent
616 Mechanism. Molecular Cancer Therapeutics. 2018;17:1781–92.

617 54. Dempster JM, Krill-Burger JM, McFarland JM, Warren A, Boehm JS, Vazquez F, et al. Gene
618 expression has more power for predicting *in vitro* cancer cell vulnerabilities than genomics
619 [Internet]. 2020 [cited 2024 Jun 26]. Available from:
620 http://biorxiv.org/lookup/doi/10.1101/2020.02.21.959627

621 55. Warren A, Chen Y, Jones A, Shibue T, Hahn WC, Boehm JS, et al. Global computational
622 alignment of tumor and cell line transcriptional profiles. Nat Commun. 2021;12:22.

623 56. Shi X, Gekas C, Verduzco D, Petiwala S, Jeffries C, Lu C, et al. Building a translational cancer
624 dependency map for The Cancer Genome Atlas. Nat Cancer. Nature Publishing Group;
625 2024;1–19.

626 57. Wang W, Albadari N, Du Y, Fowler JF, Sang HT, Xian W, et al. MDM2 Inhibitors for Cancer
627 Therapy: The Past, Present, and Future. Gottesman M, editor. Pharmacol Rev. 2024;76:414–
628 53.

629 58. Romero R, Sánchez-Rivera FJ, Westcott PMK, Mercer KL, Bhutkar A, Muir A, et al. Keap1
630 mutation renders lung adenocarcinomas dependent on Slc33a1. Nat Cancer. 2020;1:589–
631 602.

632 59. Ricketts CJ, De Cubas AA, Fan H, Smith CC, Lang M, Reznik E, et al. The Cancer Genome
633 Atlas Comprehensive Molecular Characterization of Renal Cell Carcinoma. Cell Rep.
634 2018;23:313-326.e5.

635 60. Gounder MM, Bauer TM, Schwartz GK, Weise AM, LoRusso P, Kumar P, et al. A First-in-
636 Human Phase I Study of Milademetan, an MDM2 Inhibitor, in Patients With Advanced
637 Liposarcoma, Solid Tumors, or Lymphomas. JCO. 2023;41:1714–24.

638 61. Drexler H, Fombonne S, Matsuo Y, Hu Z-B, Hamaguchi H, Uphoff C. p53 alterations in
639 human leukemia–lymphoma cell lines: in vitroartifact or prerequisite for cell
640 immortalization? Leukemia. 2000;14:198–206.

641 62. Achom M, Sadagopan A, Bao C, McBride F, Li J, Konda P, et al. A genetic basis for sex
642 differences in Xp11 translocation renal cell carcinoma. Cell [Internet]. Elsevier; 2024 [cited
643 2024 Aug 20];0. Available from: https://www.cell.com/cell/abstract/S0092-8674(24)00832-8

644 63. Maitituoheti M, Keung EZ, Tang M, Yan L, Alam H, Han G, et al. Enhancer Reprogramming
645 Confers Dependence on Glycolysis and IGF Signaling in KMT2D Mutant Melanoma. Cell Rep.
646 2020;33:108293.

647 64. Schoolmeester JK, Dao LN, Sukov WR, Wang L, Park KJ, Murali R, et al. TFE3 translocation-
648 associated perivascular epithelioid cell neoplasm (PEComa) of the gynecologic tract:
649 morphology, immunophenotype, differential diagnosis. Am J Surg Pathol. 2015;39:394–404.

650 65. Antonescu CR, Le Loarer F, Mosquera J-M, Sboner A, Zhang L, Chen C-L, et al. Novel YAP1-
651 TFE3 fusion defines a distinct subset of epithelioid hemangioendothelioma. Genes
652 Chromosomes Cancer. 2013;52:775–84.

653 66. Tanaka M, Chuaychob S, Homme M, Yamazaki Y, Lyu R, Yamashita K, et al. ASPSCR1::TFE3
654 orchestrates the angiogenic program of alveolar soft part sarcoma. Nat Commun.
655 2023;14:1957.

656 67. Wang X, Fang R, Zhang R, Ye S, Li R, Wang X, et al. Malignant melanotic Xp11 neoplasms
657 exhibit a clinicopathologic spectrum and gene expression profiling akin to alveolar soft part
658 sarcoma: a proposal for reclassification. J Pathol. 2020;251:365–77.

659 68. Lee SJ, Yang WI, Chung W-S, Kim SK. Epithelioid hemangioendotheliomas with TFE3 gene
660 translocations are compossible with CAMTA1 gene rearrangements. Oncotarget.
661 2016;7:7480–8.

662 69. Viswanathan VS, Ryan MJ, Dhruv HD, Gill S, Eichhoff OM, Seashore-Ludlow B, et al.
663 Dependency of a therapy-resistant state of cancer cells on a lipid peroxidase pathway.
664 Nature. 2017;547:453–7.

665 70. Caenepeel S, Karen R, Belmontes B, Verlinsky A, Tan H, Yang Y, et al. Abstract 6218:
666 Discovery and preclinical evaluation of AMG 397, a potent, selective and orally bioavailable
667 MCL1 inhibitor. Cancer Research. 2020;80:6218–6218.

668 71. Grubb T, Maganti S, Krill-Burger JM, Fraser C, Stransky L, Radivoyevitch T, et al. A
669 Mesenchymal Tumor Cell State Confers Increased Dependency on the BCL-XL Antiapoptotic
670 Protein in Kidney Cancer. Clin Cancer Res. 2022;28:4689–701.

671 72. Shakhova O, Zingg D, Schaefer SM, Hari L, Civenni G, Blunschi J, et al. Sox10 promotes the
672 formation and maintenance of giant congenital naevi and melanoma. Nat Cell Biol.
673 2012;14:882–90.

674 73. Cronin JC, Watkins-Chow DE, Incao A, Hasskamp JH, Schönewolf N, Aoude LG, et al. SOX10
675 ablation arrests cell cycle, induces senescence, and suppresses melanomagenesis. Cancer
676 Res. 2013;73:5709–18.

677 74. Morin PJ, Sparks AB, Korinek V, Barker N, Clevers H, Vogelstein B, et al. Activation of beta-
678 catenin-Tcf signaling in colon cancer by mutations in beta-catenin or APC. Science.
679 1997;275:1787–90.

680 75. Korinek V, Barker N, Morin PJ, van Wichen D, de Weger R, Kinzler KW, et al. Constitutive
681 transcriptional activation by a beta-catenin-Tcf complex in APC-/- colon carcinoma.
682 Science. 1997;275:1784–7.

683 76. Cancer Genome Atlas Network. Comprehensive molecular characterization of human colon
684 and rectal cancer. Nature. 2012;487:330–7.

685 77. Huang T, Hou Y, Wang X, Wang L, Yi C, Wang C, et al. Direct Interaction of Sox10 With
686 Cadherin-19 Mediates Early Sacral Neural Crest Cell Migration: Implications for Enteric
687 Nervous System Development Defects. Gastroenterology. 2022;162:179-192.e11.

688 78. Stamos JL, Weis WI. The β-catenin destruction complex. Cold Spring Harb Perspect Biol.
689 2013;5:a007898.

690 79. Kim J-S, Crooks H, Dracheva T, Nishanian TG, Singh B, Jen J, et al. Oncogenic beta-catenin is
691 required for bone morphogenetic protein 4 expression in human cancer cells. Cancer Res.
692 2002;62:2744–8.

693 80. Van Raay TJ, Fortino NJ, Miller BW, Ma H, Lau G, Li C, et al. Naked1 Antagonizes Wnt
694 Signaling by Preventing Nuclear Accumulation of β-Catenin. Koch K-W, editor. PLoS ONE.
695 2011;6:e18650.

696 81. Morrison L, Loibl S, Turner NC. The CDK4/6 inhibitor revolution — a game-changing era for
697 breast cancer treatment. Nat Rev Clin Oncol. 2024;21:89–105.

698 82. Ghandi M, Huang FW, Jané-Valbuena J, Kryukov GV, Lo CC, McDonald ER, et al. Next-
699 generation characterization of the Cancer Cell Line Encyclopedia. Nature. 2019;569:503–8.

700 83. Blache P, van de Wetering M, Duluc I, Domon C, Berta P, Freund J-N, et al. SOX9 is an
701 intestine crypt transcription factor, is regulated by the Wnt pathway, and represses the
702 CDX2 and MUC2 genes. J Cell Biol. 2004;166:37–47.

703 84. Kurnit KC, Sinno AK, Fellman BM, Varghese A, Stone R, Sood AK, et al. Effects of
704 Gastrointestinal-Type Chemotherapy in Women With Ovarian Mucinous Carcinoma. Obstet
705 Gynecol. 2019;134:1253–9.

706 85. Kurmasheva RT, Sammons M, Favours E, Wu J, Kurmashev D, Cosmopoulos K, et al. Initial
707 testing (stage 1) of tazemetostat (EPZ-6438), a novel EZH2 inhibitor, by the Pediatric
708 Preclinical Testing Program. Pediatr Blood Cancer. 2017;64.

709 86. Schmidt A, Behrendt L, Eybe J, Warmann SW, Schleicher S, Fuchs J, et al. The Effect of Direct
710 and Indirect EZH2 Inhibition in Rhabdomyosarcoma Cell Lines. Cancers (Basel). 2021;14:41.

711 87. Torchia J, Golbourn B, Feng S, Ho KC, Sin-Chan P, Vasiljevic A, et al. Integrated (epi)-
712 Genomic Analyses Identify Subgroup-Specific Therapeutic Targets in CNS Rhabdoid Tumors.
713 Cancer Cell. 2016;30:891–908.

714 88. Knutson SK, Warholic NM, Wigle TJ, Klaus CR, Allain CJ, Raimondi A, et al. Durable tumor
715 regression in genetically altered malignant rhabdoid tumors by inhibition of
716 methyltransferase EZH2. Proc Natl Acad Sci USA. 2013;110:7922–7.

717 89. Jones BA, Varambally S, Arend RC. Histone Methyltransferase EZH2: A Therapeutic Target for
718 Ovarian Cancer. Mol Cancer Ther. 2018;17:591–602.

719 90. Sasaki M, Kato D, Murakami K, Yoshida H, Takase S, Otsubo T, et al. Targeting dependency
720 on a paralog pair of CBP/p300 against de-repression of KREMEN2 in SMARCB1-deficient
721 cancers. Nat Commun. 2024;15:4770.

722 91. Voss MH, Chen D, Marker M, Hakimi AA, Lee C-H, Hsieh JJ, et al. Circulating biomarkers and
723 outcome from a randomised phase II trial of sunitinib vs everolimus for patients with
724 metastatic renal cell carcinoma. Br J Cancer. 2016;114:642–9.

725 92. Motzer RJ, Escudier B, McDermott DF, George S, Hammers HJ, Srinivas S, et al. Nivolumab
726 versus Everolimus in Advanced Renal-Cell Carcinoma. N Engl J Med. 2015;373:1803–13.

727 93. Sinha R, Winer AG, Chevinsky M, Jakubowski C, Chen Y-B, Dong Y, et al. Analysis of renal
728 cancer cell lines from two major resources enables genomics-guided cell line selection. Nat
729 Commun. Nature Publishing Group; 2017;8:15165.

730 94. Bakouny Z, Braun DA, Shukla SA, Pan W, Gao X, Hou Y, et al. Integrative molecular
731 characterization of sarcomatoid and rhabdoid renal cell carcinoma. Nature
732 Communications. Nature Publishing Group; 2021;12:808.

733 95. Maughan BL, Sirohi D. Papillary Renal Cell Carcinoma: A Review of Prospective Clinical
734 Trials. Curr Treat Options in Oncol. 2023;24:1199–212.

735 96. Henske EP, Cheng L, Hakimi AA, Choueiri TK, Braun DA. Chromophobe renal cell carcinoma.
736 Cancer Cell. 2023;41:1383–8.

737 97. Bártů M, Hojný J, Hájková N, Michálková R, Krkavcová E, Hadravský L, et al. Analysis of
738 expression, epigenetic, and genetic changes of HNF1B in 130 kidney tumours. Sci Rep.
739 2020;10:17151.

740 98. Wang C-C, Mao T-L, Yang W-C, Jeng Y-M. Underexpression of hepatocyte nuclear factor-1β
741 in chromophobe renal cell carcinoma. Histopathology. 2013;62:589–94.

742 99. Kalev P, Hyer ML, Gross S, Konteatis Z, Chen C-C, Fletcher M, et al. MAT2A Inhibition Blocks
743 the Growth of MTAP-Deleted Cancer Cells by Reducing PRMT5-Dependent mRNA Splicing
744 and Inducing DNA Damage. Cancer Cell. 2021;39:209-224.e11.

745 100. Adam J, Hatipoglu E, O'Flaherty L, Ternette N, Sahgal N, Lockstone H, et al. Renal cyst
746 formation in Fh1-deficient mice is independent of the Hif/Phd pathway: roles for fumarate in
747 KEAP1 succination and Nrf2 signaling. Cancer Cell. 2011;20:524–37.

748 101. Chen F, Zhang Y, Şenbabaoğlu Y, Ciriello G, Yang L, Reznik E, et al. Multilevel Genomics-
749 Based Taxonomy of Renal Cell Carcinoma. Cell Reports. 2016;14:2476–89.

750 102. Fabrizio FP, Costantini M, Copetti M, la Torre A, Sparaneo A, Fontana A, et al. Keap1/Nrf2
751 pathway in kidney cancer: frequent methylation of KEAP1 gene promoter in clear renal cell
752 carcinoma. Oncotarget. 2017;8:11187–98.

753 103. Pillai R, Hayashi M, Zavitsanou A-M, Papagiannakopoulos T. NRF2: KEAPing Tumors
754 Protected. Cancer Discovery. 2022;12:625–43.

755 104. M G, T P, L B-P. Reductive stress in cancer: coming out of the shadows. Trends in cancer
756 [Internet]. Trends Cancer; 2024 [cited 2024 Feb 28];10. Available from:
757 https://pubmed.ncbi.nlm.nih.gov/37925319/

758 105. Weiss-Sadan T, Ge M, Hayashi M, Gohar M, Yao C-H, de Groot A, et al. NRF2 activation
759 induces NADH-reductive stress, providing a metabolic vulnerability in lung cancer. Cell
760 Metabolism. 2023;S1550413123000128.

761 106. Köferle A, Schlattl A, Hörmann A, Thatikonda V, Popa A, Spreitzer F, et al. Interrogation of
762 cancer gene dependencies reveals paralog interactions of autosome and sex chromosome-
763 encoded genes. Cell Rep. 2022;39:110636.

764 107. Qi M, Pang J, Mitsiades I, Lane AA, Rheinbay E. Loss of chromosome Y in primary tumors.
765 Cell. 2023;S0092-8674(23)00646-3.

766 108. Donehower LA, Soussi T, Korkut A, Liu Y, Schultz A, Cardenas M, et al. Integrated Analysis of
767 TP53 Gene and Pathway Alterations in The Cancer Genome Atlas. Cell Rep. 2019;28:1370-
768 1384.e5.

769 109. Zou Y, Palte MJ, Deik AA, Li H, Eaton JK, Wang W, et al. A GPX4-dependent cancer cell state
770 underlies the clear-cell morphology and confers sensitivity to ferroptosis. Nat Commun.
771 Nature Publishing Group; 2019;10:1617.

772 110. Mavrakis KJ, McDonald ER, Schlabach MR, Billy E, Hoffman GR, deWeck A, et al. Disordered
773 methionine metabolism in MTAP/CDKN2A-deleted cancers leads to dependence on PRMT5.
774 Science. American Association for the Advancement of Science; 2016;351:1208–13.

775 111. Kryukov GV, Wilson FH, Ruth JR, Paulk J, Tsherniak A, Marlow SE, et al. MTAP deletion
776 confers enhanced dependency on the PRMT5 arginine methyltransferase in cancer cells.
777 Science. American Association for the Advancement of Science; 2016;351:1214–8.

778 112. Ronk H, Rosenblum JS, Kung T, Zhuang Z. Targeting PP2A for cancer therapeutic modulation.
779 Cancer Biol Med. 2022;19:1428–39.

780 113. Ho WS, Wang H, Maggio D, Kovach JS, Zhang Q, Song Q, et al. Pharmacologic inhibition of
781 protein phosphatase-2A achieves durable immune-mediated antitumor activity when
782 combined with PD-1 blockade. Nat Commun. 2018;9:2126.

783 114. Steingrímsson E, Tessarollo L, Pathak B, Hou L, Arnheiter H, Copeland NG, et al. Mitf and
784 Tfe3, two members of the Mitf-Tfe family of bHLH-Zip transcription factors, have important
785 but functionally redundant roles in osteoclast development. PNAS. National Academy of
786 Sciences; 2002;99:4477–82.

787 115. Pastore N, Vainshtein A, Klisch TJ, Armani A, Huynh T, Herz NJ, et al. TFE3 regulates whole-
788 body energy metabolism in cooperation with TFEB. EMBO Mol Med. 2017;9:605–21.

789 116. Settembre C, De Cegli R, Mansueto G, Saha PK, Vetrini F, Visvikis O, et al. TFEB controls
790 cellular lipid metabolism through a starvation-induced autoregulatory loop. Nat Cell Biol.
791 2013;15:647–58.

792 117. Raben N, Puertollano R. TFEB and TFE3: Linking Lysosomes to Cellular Adaptation to Stress.
793 Annu Rev Cell Dev Biol. 2016;32:255–78.

794 118. Chiu Y-C, Zheng S, Wang L-J, Iskra BS, Rao MK, Houghton PJ, et al. Predicting and
795 characterizing a cancer dependency map of tumors with deep learning. Sci Adv.
796 2021;7:eabh1275.

797 119. Yuda J, Will C, Phillips DC, Abraham L, Alvey C, Avigdor A, et al. Selective MCL-1 inhibitor
798 ABBV-467 is efficacious in tumor models but is associated with cardiac troponin increases
799 in patients. Commun Med. 2023;3:154.

800 120. Rauh U, Wei G, Serrano-Wu M, Kosmidis G, Kaulfuss S, Siegel F, et al. BRD-810 is a highly
801 selective MCL1 inhibitor with optimized in vivo clearance and robust efficacy in solid and
802 hematological tumor models. Nat Cancer [Internet]. 2024 [cited 2024 Sep 5]; Available from:
803 https://www.nature.com/articles/s43018-024-00814-0

804 121. Msaouel P, Genovese G, Tannir NM. Renal Cell Carcinoma of Variant Histology: Biology and
805 Therapies. Hematol Oncol Clin North Am. 2023;S0889-8588(23)00053-9.

806 122. Msaouel P, Malouf GG, Su X, Yao H, Tripathi DN, Soeung M, et al. Comprehensive Molecular
807 Characterization Identifies Distinct Genomic and Immune Hallmarks of Renal Medullary
808 Carcinoma. Cancer Cell. 2020;37:720-734.e13.

809 123. Coutinho DF, Mundi PS, Marks LJ, Burke C, Ortiz MV, Diolaiti D, et al. Validation of a non-
810 oncogene encoded vulnerability to exportin 1 inhibition in pediatric renal tumors. Med.
811 2022;3:774-791.e7.

812 124. Wang J, Papanicolau-Sengos A, Chintala S, Wei L, Liu B, Hu Q, et al. Collecting duct
813 carcinoma of the kidney is associated with CDKN2A deletion and SLC family gene up-
814 regulation. Oncotarget. 2016;7:29901–15.

815 125. Doench JG, Hartenian E, Graham DB, Tothova Z, Hegde M, Smith I, et al. Rational design of
816 highly active sgRNAs for CRISPR-Cas9–mediated gene inactivation. Nat Biotechnol.
817 2014;32:1262–7.

818 126. Doench JG, Fusi N, Sullender M, Hegde M, Vaimberg EW, Donovan KF, et al. Optimized
819 sgRNA design to maximize activity and minimize off-target effects of CRISPR-Cas9. Nat
820 Biotechnol. 2016;34:184–91.

821 127. Sanson KR, Hanna RE, Hegde M, Donovan KF, Strand C, Sullender ME, et al. Optimized
822 libraries for CRISPR-Cas9 genetic screens with multiple modalities. Nat Commun.
823 2018;9:5416.

824 128. Shalem O, Sanjana NE, Hartenian E, Shi X, Scott DA, Mikkelsen TS, et al. Genome-Scale
825 CRISPR-Cas9 Knockout Screening in Human Cells. Science. 2014;343:84–7.

826 129. Sanjana NE, Shalem O, Zhang F. Improved vectors and genome-wide libraries for CRISPR
827 screening. Nat Methods. 2014;11:783–4.

828 130. Li W, Xu H, Xiao T, Cong L, Love MI, Zhang F, et al. MAGeCK enables robust identification of
829 essential genes from genome-scale CRISPR/Cas9 knockout screens. Genome Biol.
830 2014;15:554.

831 131. Li H, Durbin R. Fast and accurate short read alignment with Burrows-Wheeler transform.
832 Bioinformatics. 2009;25:1754–60.

833 132. Riester M, Singh AP, Brannon AR, Yu K, Campbell CD, Chiang DY, et al. PureCN: copy
834 number calling and SNV classification using targeted short read sequencing. Source Code
835 Biol Med. 2016;11:13.

836 133. Li B, Dewey CN. RSEM: accurate transcript quantification from RNA-Seq data with or without
837 a reference genome. BMC Bioinformatics. 2011;12:323.

838 134. Dobin A, Davis CA, Schlesinger F, Drenkow J, Zaleski C, Jha S, et al. STAR: ultrafast universal
839 RNA-seq aligner. Bioinformatics. 2013;29:15–21.

840 135. Tatlow PJ, Piccolo SR. A cloud-based workflow to quantify transcript-expression levels in
841 public cancer compendia. Sci Rep. 2016;6:39259.

842 136. Zhang Y, Parmigiani G, Johnson WE. ComBat-seq: batch effect adjustment for RNA-seq
843 count data. NAR Genom Bioinform. 2020;2:lqaa078.

844 137. Braun DA, Hou Y, Bakouny Z, Ficial M, Sant' Angelo M, Forman J, et al. Interplay of somatic
845 alterations and immune infiltration modulates response to PD-1 blockade in advanced clear
846 cell renal cell carcinoma. Nat Med. Nature Publishing Group; 2020;26:909–18.

847 138. Davidson-Pilon C. lifelines: survival analysis in Python. Journal of Open Source Software.
848 2019;4:1317.

849 139. Seavey CN, Pobbati AV, Hallett A, Ma S, Reynolds JP, Kanai R, et al. WWTR1(TAZ)-CAMTA1
850 gene fusion is sufficient to dysregulate YAP/TAZ signaling and drive epithelioid
851 hemangioendothelioma tumorigenesis. Genes Dev. 2021;35:512–27.

852 140. Braun DA, Ishii Y, Walsh AM, Van Allen EM, Wu CJ, Shukla SA, et al. Clinical Validation of
853 *PBRM1* Alterations as a Marker of Immune Checkpoint Inhibitor Response in Renal Cell
854 Carcinoma. JAMA Oncol. 2019;5:1631.

855 141. Motzer RJ, Tannir NM, McDermott DF, Arén Frontera O, Melichar B, Choueiri TK, et al.
856 Nivolumab plus Ipilimumab versus Sunitinib in Advanced Renal-Cell Carcinoma. N Engl J
857 Med. 2018;378:1277–90.

858 142. Cancer Genome Atlas Research Network, Weinstein JN, Collisson EA, Mills GB, Shaw KRM,
859 Ozenberger BA, et al. The Cancer Genome Atlas Pan-Cancer analysis project. Nat Genet.
860 2013;45:1113–20.

861 143. Cancer Genome Atlas Research Network, Linehan WM, Spellman PT, Ricketts CJ, Creighton
862 CJ, Fei SS, et al. Comprehensive Molecular Characterization of Papillary Renal-Cell
863 Carcinoma. N Engl J Med. 2016;374:135–45.

144. Davis CF, Ricketts CJ, Wang M, Yang L, Cherniack AD, Shen H, et al. The somatic genomic landscape of chromophobe renal cell carcinoma. Cancer Cell. 2014;26:319–30.

145. Liu YJ, Ussakli C, Antic T, Liu Y, Wu Y, True L, et al. Sporadic oncocytic tumors with features intermediate between oncocytoma and chromophobe renal cell carcinoma: comprehensive clinicopathological and genomic profiling. Hum Pathol. 2020;104:18–29.

Acknowledgements:

Schematic illustrations were created with BioRender.com.

Funding: S.R.V: Doris Duke Charitable Foundation (Clinician-Scientist Development Award grant number: 2020101), Department of Defense Kidney Cancer Research Program (DoD KCRP) (W81XWH-19-1-0815 / KC180130; W81XWH-22-1-1016 / KC210039), NCI (R01CA286652; R01CA279044; R01CA269505), DF/HCC Kidney SPORE (2P50CA101942-16), Rally Foundation Independent Investigator Grant (23IN3). J.L.: Department of Defense Kidney Cancer Research Program (DoD KCRP) (W81XWH-22-1-0399). P.K. Department of Defense Kidney Cancer Research Program (DoD KCRP) Postdoctoral and Clinical Fellowship (HT94252310066). C.N.W.: American Association for Cancer Research (AACR) Exelixis Renal Cell Carcinoma Research Fellowship (1306525). T.K.C.: Dana-Farber/Harvard Cancer Center Kidney SPORE (2P50CA101942-16) and Program 5P30CA00651656, the Kohlberg Chair at Harvard Medical School and the Trust Family, Michael Brigham, Pan Mass Challenge, Hinda and Arthur Marcus Fund, and Loker Pinard Funds for Kidney Cancer Research at DFCI.

Author contributions: S.R.V designed and supervised the study. B.L., A.S., S.R.V wrote the manuscript with input from all co-authors. A.S. performed analysis of genome-scale CRISPR screening data, dependency prediction and developed the predictive model used in this study. Y.C. and P.K. assisted in analysis of dependency data. B.L. led experimental work including genome-scale CRISPR screening and dependency validation. J.L., C.N.W., Y.W. assisted in experimental work and contributed to experimental design. T.K.C., A.S., provided clinical trial data and/or analysis. J.G.D. contributed to design of screening and validation studies.

Data Availability: Chronos scores from tRCC CRISPR screen are available in **Supplementary Table S1.** External datasets analyzed are public and are available from the respective cited publications. Chronos score predictions for all external datasets are available in **Supplementary Table S4.**

Code Availability: Code for the developed tool will be publicly available in Github at time of publication: https://github.com/SViswanathanLab/TrPLet.

Declaration of Interests: Aspects of this work are the subject of a pending patent application (A.S., S.R.V.). S.R.V.: has consulted for Jnana Therapeutics within the past 3 years; receives research support from Bayer. T.K.C. reports institutional and personal paid or unpaid support for research, advisory board participation, consultancy, and honoraria within the past 5 years from Alkermes, Arcus Bio, AstraZeneca, Aravive, Aveo, Bayer, Bristol Myers Squibb, Calithera, Circle Pharma, Deciphera Pharmaceuticals, Eisai, EMD Serono, Exelixis, GlaxoSmithKline, Gilead, HiberCell, IQVIA, Infinity, Ipsen, Jansen, Kanaph, Lilly, Merck, Nikang, Neomorph, Nuscan and Precede Bio, Novartis, Oncohost, Pfizer, Roche, Sanofi Aventis, Scholar Rock, Surface Oncology, Takeda, and Tempest and equity in Tempest, Pionyr, Osel, Precede Bio, CureResponse, InnDura Therapeutics, and Primium.

List of Supplementary Materials

Materials and Methods

Supplementary Fig. S1 to Fig. S6
Supplementary Table S1 to Table S4
References 125-145

Main Figures and Captions

Fig.1 | Genome-scale genetic screening reveals selective essentialities of tRCC cells

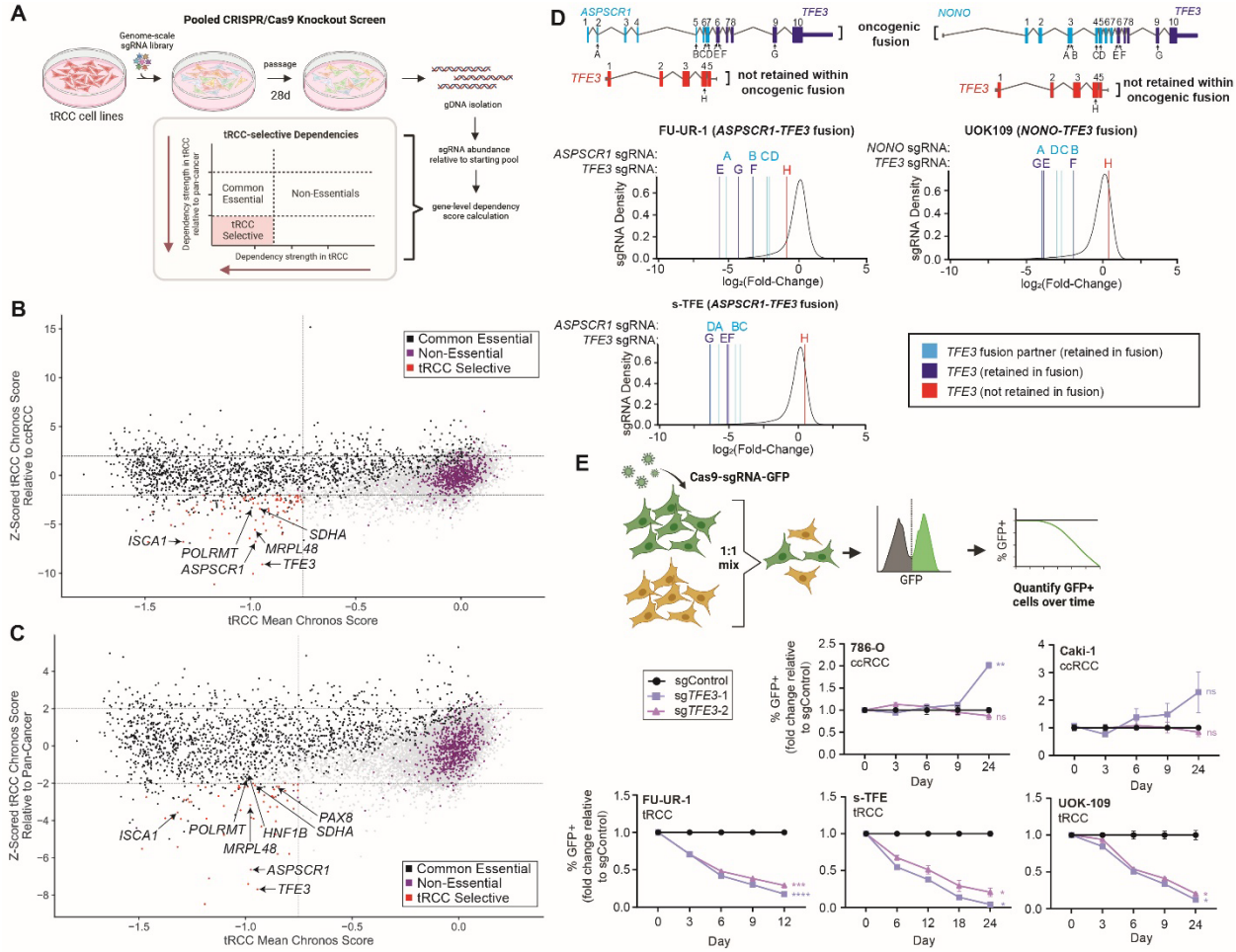

(A) Workflow for CRISPR screens and analysis to identify tRCC-selective genetic dependencies.

(B-C) Landscape of tRCC-selective dependencies. Mean Chronos score for each gene across the 3 tRCC cell lines screened in this study is plotted against the Z-scored Chronos score for that gene (Z-score calculated relative to DepMap ccRCC cell lines in **B** and relative to all DepMap cell lines in **C**). Non-essential-genes are colored in purple while common essential genes are colored in black (42). tRCC-selective dependencies (defined as Z-score < -2; absolute Chronos score < -0.75) are colored in red.

(D) Log-fold change for individual sgRNAs targeting either *TFE3* (E, F, G, H) or fusion partner (A, B, C, D) in tRCC CRISPR screens. The exons targeted by each sgRNA are indicated in the schematics. For each cell line, the top schematic represents the exons coding for the oncogenic fusion while the bottom schematic represents the N-terminal exons of *TFE3* not included in the oncogenic fusion. Density plot shows the distribution for LFC of all sgRNAs assessed in the CRISPR screen in each cell line while vertical lines represent log-fold change for individual sgRNAs. Note: Figure shows the *ASPSCR1-TFE3* fusion in s-TFE cells; the *ASPSCR1-TFE3* fusion in FU-UR-1 cells retains exon 5 of *TFE3* exon 5.

(E) Competitive growth assay to assess the effects of *TFE3* knockout in two ccRCC lines (786-O, Caki-1) and three tRCC lines (UOK109, FU-UR-1, s-TFE). Cells expressing Cas9/sgRNA and GFP were mixed in a 1:1 ratio

930 with parental cells and proportion relative to sgControl cells was calculated at each time point via flow
931 cytometry. Shown as mean +/- s.d., n=2 biological replicates per condition. *P*-values were calculated by
932 Welch's (two-tailed unpaired) t-test as compared with sgControl samples at the final time point. *$P < 0.05$, **P
933 < 0.01, ***$P < 0.001$, ****$P < 0.0001$.

934

Fig.2 | Validation of selective tRCC dependencies

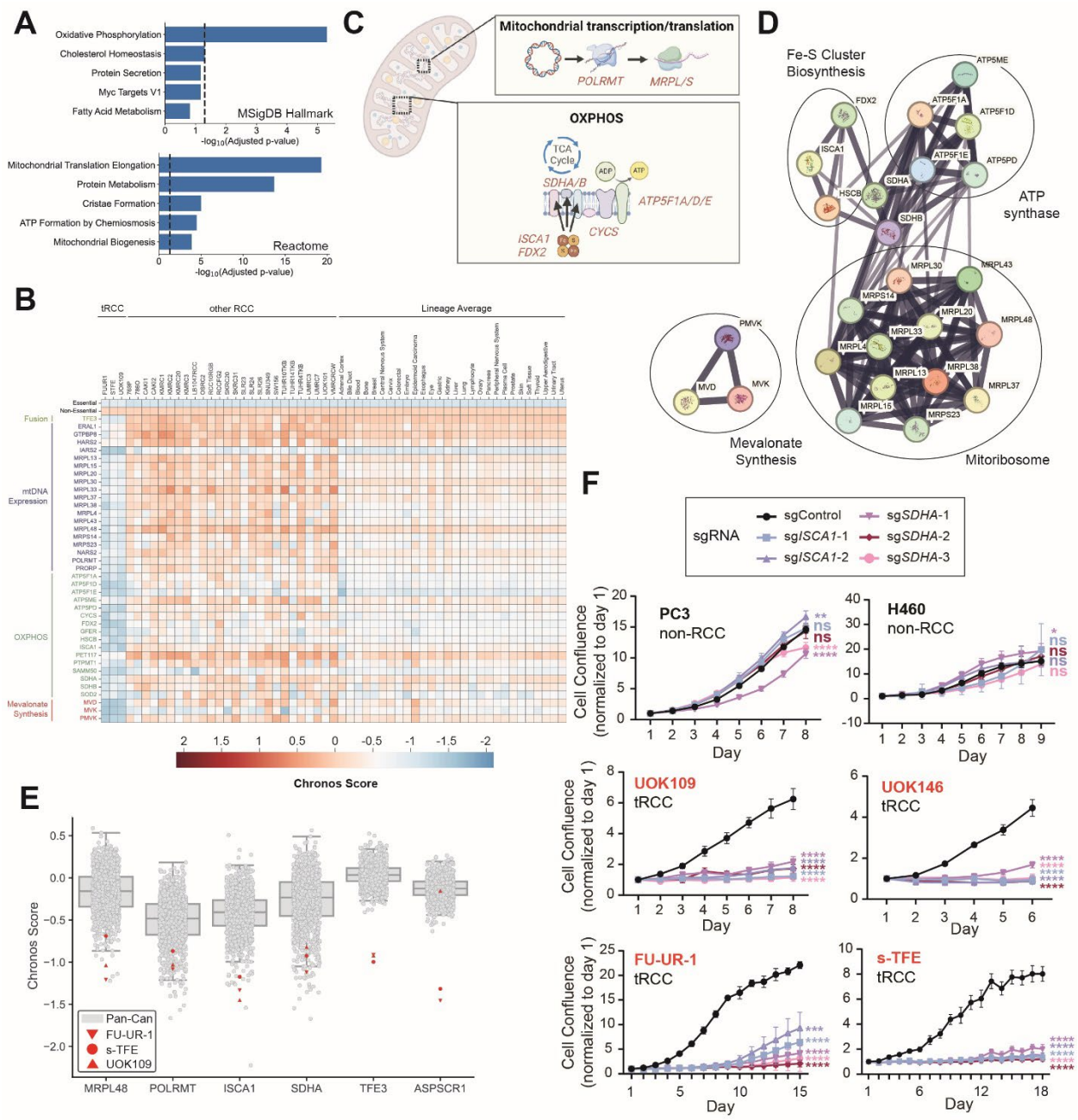

(A) Pathway enrichment (Enrichr) on gene dependencies shared across all three tRCC cell lines (defined as genes with ΔChronos ≤ -0.5 between every tRCC cell line and DepMap ccRCC mean).

(B) Heat map of tRCC-selective dependencies (defined as genes with ΔChronos ≤ -0.5 between every tRCC cell line and DepMap ccRCC mean), for selected pathways (remaining genes/pathways shown in **Supplementary Fig. S1B**). Chronos scores for individual tRCC cell lines, DepMap RCC cell lines, and average Chronos score for each of 28 lineages screened in DepMap are shown. The top two rows indicate mean Chronos scores for essential and non-essential genes in each column, shown for reference.

(C) Schematic depicting tRCC-selective dependencies that fall within pathways related to mitochondrial metabolism.

(D) Protein-protein interaction network amongst interacting tRCC-selective gene dependencies (genes with ΔChronos ≤ -0.5 between every tRCC cell line and DepMap ccRCC mean) involved in mtDNA expression, OXPHOS, and mevalonate synthesis (STRINGdb).

(E) Distribution of Chronos scores for indicated genes (*POLRMT*, *MRPL48*, *ISCA1, SDHA, TFE3, ASPSCR1*) across all DepMap cell lines (gray) and tRCC cell lines screened in this study (red).

(F) Relative confluence of non-RCC cells (PC3, H460), and tRCC cells (UOK109, UOK146, FU-UR-1, s-TFE) after infection with lentivirus expressing Cas9 and either non-targeting control sgRNA, *ISCA1* sgRNAs, or *SDHA* sgRNAs. Confluence was normalized to day 1, shown as mean +/- s.d., n=6 biological replicates per condition. *P*-values were calculated by Welch's (two-tailed unpaired) t test as compared with sgControl samples for the last assay day. *$P < 0.05$, **$P < 0.01$, ***$P < 0.001$, ****$P < 0.0001$.

Fig.3 | A machine-learning model uncovers additional strong dependencies in tRCC subsets

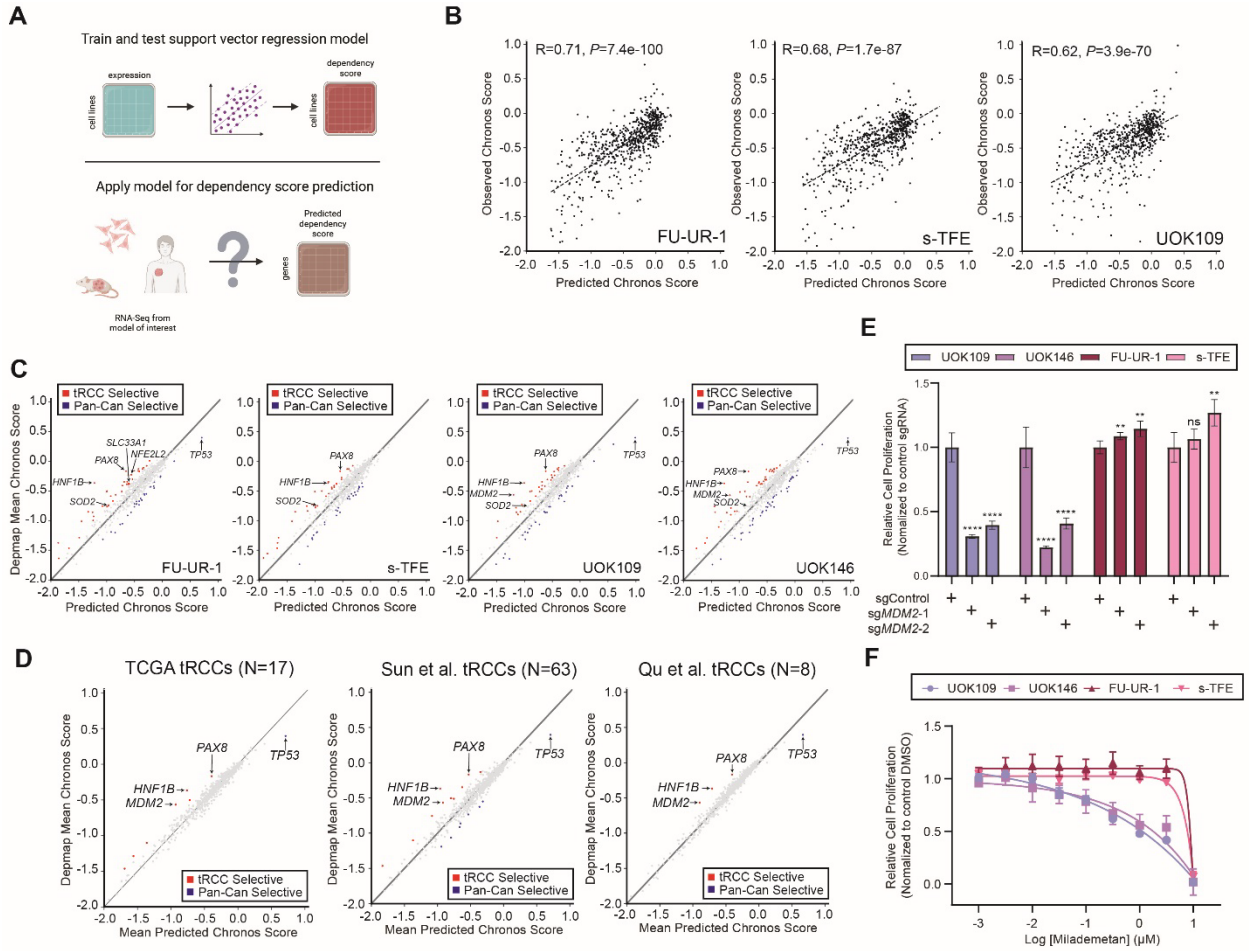

(A) Schematic of machine learning approach used to nominate candidate vulnerabilities in cell lines or tumors based on RNA-Seq profile.

(B) Correlation between observed Chronos score from CRISPR screen performed in this study and Chronos score predicted by our model, for 645 dependencies across three tRCC cell lines (FU-UR-1, S-TFE, UOK109; *Note*: discrepancy in number of genes predicted (N=657) and plotted (N=645) due to imperfect overlap in genes screened between Avana [DepMap] and Brunello libraries [tRCC screen]). *P*-values calculated from Pearson's correlation test.

(C) tRCC-selective dependencies based on predicted Chronos scores across four tRCC cell lines, including one line (UOK146) that was not assessed by genome-scale CRISPR screening. In each cell line, predicted Chronos scores in the tRCC cell line are plotted against mean Chronos score across all DepMap cell lines (as experimentally determined by genome-scale CRISPR screening). Red: ΔChronos ≤ -0.2; blue: ΔChronos ≥ 0.2 between predicted and DepMap mean.

(D) tRCC-selective dependencies based on mean predicted Chronos scores for 657 genes across tRCC tumors in three independent cohorts, as compared with mean Chronos score across all DepMap cell lines (red: ΔChronos ≤ -0.2; blue: ΔChronos ≥ 0.2 between mean predicted and DepMap mean Chronos scores).

976 **(E)** Relative viability of tRCC cells (UOK109, UOK146, FU-UR-1, s-TFE) after CRISPR/Cas9 knockout of *MDM2*.
977 Viability is normalized to control sgRNA, shown as mean +/- s.d., n=6 biological replicates per condition. *P*-
978 values were calculated by Welch's (two-tailed unpaired) t test as compared with sgControl samples. *$P < 0.05$,
979 **$P < 0.01$, ***$P < 0.001$, ****$P < 0.0001$.

980 **(F)** Viability of tRCC cell lines treated with indicated concentrations of milademetan (MDM2 inhibitor) and
981 assayed for cell viability after 3 days with CellTiter-Glo. Viability at each concentration is relative to vehicle-
982 treated cells, shown as mean +/- s.d., n=6 biological replicates.

983

Fig.4 | Predicting and validating dependencies in ASPS

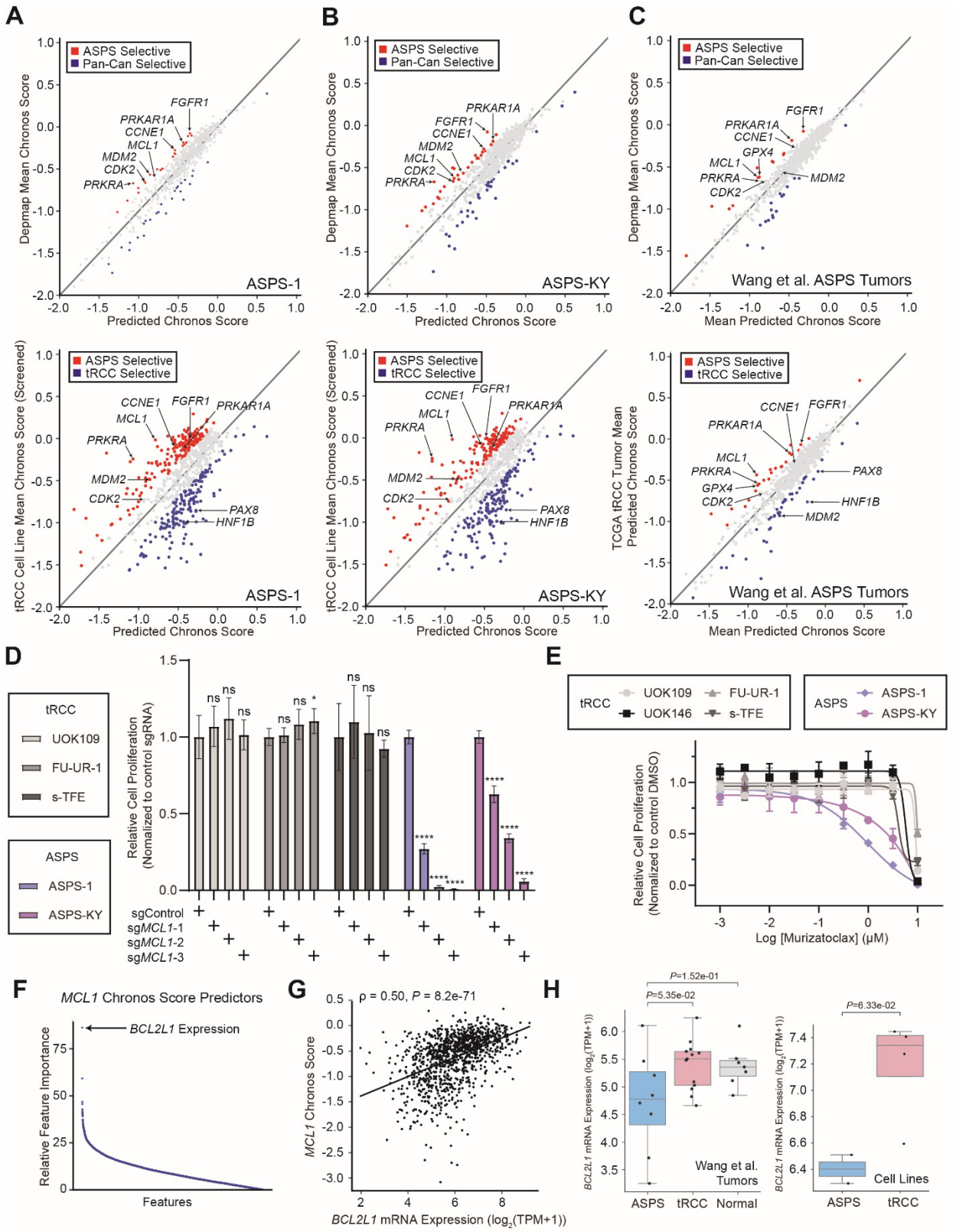

987 **(A-C)** Selective dependencies in ASPS cell lines(ASPS-1 **(A)**, ASPS-KY **(B)**) or ASPS tumors (**(C)**, profiled by
988 RNA-Seq in a prior study (67)) based on their (mean) predicted Chronos scores as compared with mean
989 Chronos score across all DepMap cell lines (top panels) or tRCC cell lines/TCGA tRCC tumors that were
990 screened/predicted in this study (bottom panels). Red: ΔChronos ≤ -0.2; blue: ΔChronos ≥ 0.2 between
991 (mean) predicted Chronos score and DepMap mean (top) or tRCC cell line/TCGA tRCC tumor mean (bottom).

992 **(D)** Proliferation of ASPS cell lines transduced with one of 3 distinct sgRNAs targeting *MCL1* or a non-targeting
993 sgRNA control. Shown as mean +/- s.d., n = 6 biological replicates per condition. *P*-values were calculated by
994 Welch's t-test (two-tailed unpaired) as compared with sgControl samples. *$P < 0.05$, **$P < 0.01$, ***$P <$
995 0.001, ****$P < 0.0001$.

996 **(E)** Viability of ASPS-1 and ASPS-KY and non-ASPS (versus tRCC) cell lines treated with indicated
997 concentrations of murizatoclax (MCL1 inhibitor) and assayed for cell viability after 3 days with CellTiter-Glo.
998 Viability at each concentration is relative to vehicle-treated cells, shown as mean +/- s.d., n=3 replicates.

999 **(F)** Relative feature importance (ranked across top 5000 features) for RNA predictors of *MCL1* Chronos score.
1000 Each point represents an individual feature (see **Methods**).

1001 **(G)** *MCL1* Chronos score is plotted against *BCL2L1* mRNA expression ($\log_2$(TPM+1)) across all DepMap cell
1002 lines.

1003 **(H)** *BCL2L1* mRNA expression ($\log_2$(TPM+1)) in ASPS tumors, tRCC tumors, and kidney-adjacent normal
1004 tissue from Wang et al. (67) (left) as well as ASPS cell lines (ASPS-1, ASPS-KY) and tRCC cell lines (FU-UR-1,
1005 s-TFE, UOK109, UOK146) (right) profiled by RNA-seq are shown. *P*-values computed by Welch's (two-tailed
1006 unpaired) t-test.

1007

1008 **Fig.5 | A landscape of candidate dependencies across TCGA**

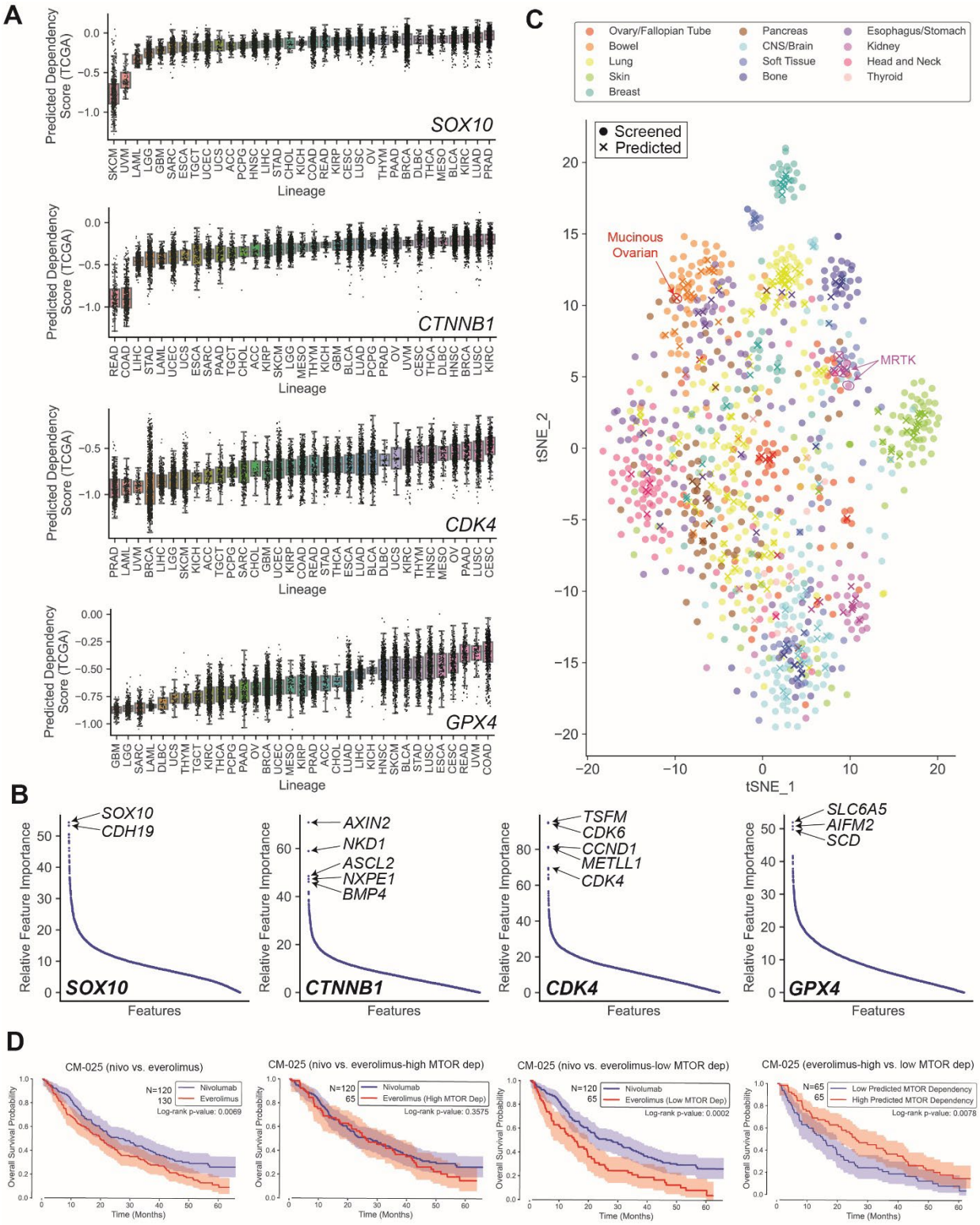

1009

1010

1011 **(A)** Predicted Chronos scores for *SOX10*, *CTNNB1*, *CDK4* and *GPX*4 across tumor types profiled in TCGA;
1012 tumors grouped by TCGA lineage.
1013 **(B)** Relative feature importance (ranked across top 5000 features) for RNA predictors of *SOX10*, *CTNNB1*,
1014 *CDK4* and *GPX*4 Chronos scores. Each point represents an individual feature (see **Methods**).
1015 **(C)** *t*-SNE projection based on dependency score for cell lines experimentally screened in the DepMap
1016 (N=833, circle) or cell lines for which dependencies for 657 PD genes were predicted by our model (N=251
1017 cell lines, cross). Cell lines are colored based on annotated lineage, with 13 common lineages plotted
1018 (lineages with ≥10 predicted cell lines; hematological lineages and fibroblasts removed). Selected cell lines
1019 whose dependency predictions diverge from the parental lineage are highlighted.
1020 **(D)** Overall survival (OS) for ccRCC patients on clinical trial of nivolumab vs. everolimus (CM-025). From left
1021 to right: nivolumab vs. everolimus in the overall population; nivolumab vs. everolimus-treated patients with
1022 high predicted *MTOR* dependency; nivolumab vs. everolimus-treated patients with low predicted *MTOR*
1023 dependency; everolimus-treated patients with high vs. low predicted *MTOR* dependency. *P*-values
1024 calculated by log-rank test.
1025

Fig.6 | A landscape of candidate dependencies across rare kidney cancers

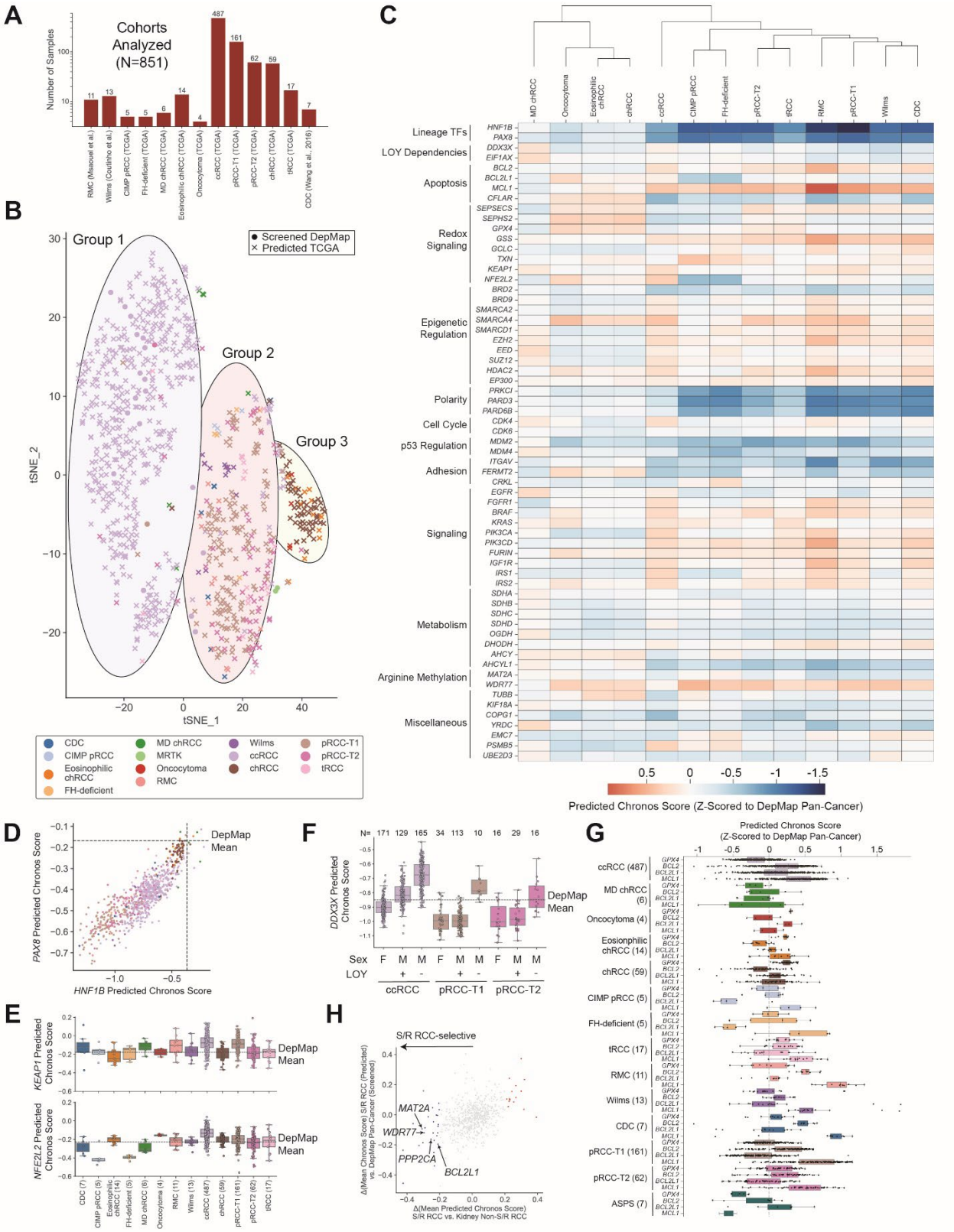

1029 **(A)** RNA-Seq data from 851 renal tumor-derived samples was curated from across 4 published datasets
1030 (59,122–124), representing 13 distinct types of kidney cancer. The number of samples for each kidney cancer
1031 subtype is shown.

1032 **(B)** *t*-SNE projection based on dependency score for kidney tumors with dependencies predicted by our model
1033 (N=851, cross) and kidney cancer cell lines experimentally screened in the DepMap (N=22), across 657 PD
1034 genes. Tumors are colored based on annotated subtype and three groups are outlined.

1035 **(C)** Heatmap of predicted Chronos score (Z-scored to DepMap pan-cancer value for screened cell lines) for
1036 63 curated dependencies, including those selective in one or more subtypes of kidney cancer (relative to
1037 pan-cancer) or additional actionable dependencies with small molecule inhibitors. Individual kidney tumor
1038 subtypes are as in **Fig.6A-B**. Hierarchical clustering is based on genes shown in the heatmap.

1039 **(D)** Scatter plot of predicted *HNF1B* Chronos score versus predicted *PAX8* Chronos score for individual
1040 kidney tumors (N=851), colored by subtype as indicated in **Fig.6B**. DepMap mean Chronos score for each of
1041 these genes across experimentally screened cell lines is indicated by dotted lines.

1042 **(E)** Box plot of predicted *KEAP1* (top) and *NFE2L2* (bottom) Chronos score for individual kidney tumors
1043 (N=851), grouped by subtype indicated in **Fig.6A-B**. Mean Chronos score in DepMap (experimentally derived)
1044 for these genes are indicated by dotted lines. All box plots are shown with median, upper and lower quartile
1045 lines, and extend to [Q1-1.5xIQR, Q3+1.5xIQR].

1046 **(F)** Box plot of predicted *DDX3X* Chronos score across ccRCC, pRCC-T1, and pRCC-T2 tumors in TCGA
1047 stratified by annotated sex and loss of chrY (LOY) status (107). Experimentally derived mean Chronos score
1048 for *DDX3X* in DepMap is indicated as a dotted line.

1049 **(G)** Box plot of predicted *GPX4*, *BCL2*, *BCL2L1*, and *MCL1* Chronos score (Z-scored to DepMap pan-cancer)
1050 for individual kidney tumors (N=851), grouped by subtype indicated in **Fig.6A**. DepMap mean (Z=0) is
1051 indicated as a dotted line. Predictions for ASPS, which was experimentally confirmed to be *MCL1* dependent
1052 (**Fig.4**) are also shown as reference.

1053 **(H)** Predicted dependency scores for S/R RCCs vs. non-S/R RCCs in TCGA (94). Difference in mean predicted
1054 Chronos score between S/R RCCs and non-S/R RCCs is plotted against the difference in mean Chronos
1055 score between S/R RCCs (predicted) and the DepMap pan-cancer mean. Points are colored based on the
1056 comparison between S/R RCCs and non-S/R RCCs (blue: ΔChronos $\leq$ -0.2, $P < 0.05$; red: ΔChronos $\geq$ 0.2, $P <$
1057 0.05 from Welch's two-tailed unpaired t-test).

1058 ## Methods

1059 **Cell lines**
1060 H460 (ATCC® HTB-177; RRID:CVCL_0459), PC3 (ATCC® CRL-1435, RRID:CVCL_0035), 786-O (ATCC® CRL-
1061 1932™; RRID:CVCL_1051), 293T (ATCC® CRL-11268™; RRID:CVCL_0063), Caki-1 (ATCC® HTB-46™;
1062 RRID:CVCL_0234), UOK109 (Dr. W. Marston Linehan's laboratory, National Cancer Institute;
1063 RRID:CVCL_B087), UOK146 (Dr. W. Marston Linehan's laboratory, National Cancer Institute,
1064 RRID:CVCL_B123), s-TFE (RIKEN, #RCB4699, RRID:CVCL_R854), ASPS-1 (Dr. Robert H Shoemaker's
1065 laboratory, National Cancer Institute; RRID:CVCL_S738), and ASPS-KY (RIKEN, #RCB5683, RRID:CVCL_S737)
1066 cell lines were cultured at 37°C in DMEM with 10% FBS, 100 U/mL penicillin, and 100 µg/mL Normocin
1067 (#NC9390718). The FU-UR-1 (Dr. Masako Ishiguro's laboratory, Fukuoka University School of Medicine,
1068 RRID:CVCL_6997) cell line was cultured at 37°C in DMEM/F12 (1:1) with 10% FBS, 100 U/mL penicillin, and 100
1069 µg/mL Normocin.

1070 **Genome-scale CRISPR knockout screens**
1071 For the UOK109, FU-UR-1, and s-TFE cell lines, Cas9-expressing cells were constructed as follows: each
1072 parental cell line was seeded in 12-well plates (2.5 × 10^5 cells/well) and incubated at 37°C overnight. The
1073 following day, the medium was replaced, and cells were incubated with lentivirus corresponding to the
1074 pLX_311-Cas9 plasmid (RRID:Addgene_96924), which encodes the Cas9 protein, and 0.8 µg/mL polybrene.
1075 After overnight incubation at 37°C, the cells were trypsinized the following day and cultured in selective media
1076 containing 5 µg/mL blasticidin. After selection, Cas9 expression and activity were confirmed in each
1077 transduced cell line via western blotting and a Cas9-activity assay as described in a previous reference (125).

1078 The Broad Institute Brunello sgRNA library (77,441 sgRNAs targeting 19,114 genes with 1,000 non-targeting
1079 control sgRNAs) was applied for the CRISPR Screen (126,127). UOK109, FU-UR-1, and s-TFE cells were seeded
1080 into 12-well plates at a density of 1.5/1.25/1.5 x 10^6 cells/well, with 1.2 µg/mL polybrene and virus titrated at
1081 MOI <0.3 and spun at 1000 xg for 2 hours at 33°C. After spinfection, 1 mL medium was added to each well and
1082 incubated at 37°C overnight. The following day, all cells were trypsinized and expanded into 15 cm plates at 4
1083 x 10^6 cells/plate with 4/5/5 µg/mL puromycin for a week. Medium with puromycin was replaced every 3 days.
1084 After puromycin selection, cells were seeded at 3 x 10^6 cells/plate and replated every 7 days in 15 cm plates
1085 for 21 days. At 28 days post-infection, cells were collected and stored at -20°C before genomic DNA was
1086 collected.

1087 Genomic DNA was collected with Takara NucleoSpin Blood Kits (Macherey-Nagel), following the
1088 manufacturer's protocol. Before sequencing, genomic DNA samples were amplified by PCR.

1089 **Lentiviral production**
1090 All sgRNAs were cloned into plentiCRISPRv2 (RRID:Addgene_52961, puromycin resistance) as described
1091 (128,129). Sequence of primers for sgRNA cloning are listed in **Supplementary Table S2**. All the constructs
1092 were confirmed by Sanger sequencing.

1093 Lentivirus was prepared by transfecting 293T cells with three plasmids: plentiCRISPRv2
1094 (RRID:Addgene_86153), psPAX2 (RRID:Addgene_12260), and pMD2.G (RRID:Addgene_12259) using
1095 polyethylenimine (PEI). Media was replaced with standard growth media after 12 hours, and supernatant
1096 containing the virus was collected 48 hours post-transfection.

1097 **Validation of genome-scale CRISPR-Cas9 screens and dependency predictions**

1098 PC3, H460, Caki-1, 786-O, UOK109, UOK146, FU-UR-1, s-TFE, and ASPS-1 cell lines were transduced with
1099 lentivirus expressing CRISPR-Cas9 and sgRNA targeting the gene of interest, selected by puromycin, and then
1100 seeded in 96-well plates for confluence and proliferation assays with cell densities of 400-2,000 cells/well
1101 depending on the cell line. On days 7-28, depending on the cell line, cell growth medium was removed from

1102 the plates and the Cell Titer Glo reagent (Promega, #G7571) was added following the user's instructions. Plates
1103 were then shaken at room temperature for 10 minutes. Luminescence was measured on a SpectraMax plate
1104 reader. For cell confluence assays, cell confluence on each plate was determined using a Celigo Imaging
1105 Cytometer daily.

1106 For drug assays, cells were incubated with milademetan (MCE: #HY-101266) or murizatoclax (MCE: #HY-
1107 109184) for 3 days as indicated. Cell Titer Glo assay was measured using a SpectraMax plate reader.

1108 **Competition assay**
1109 Caki-1, 786-O, UOK109, FU-UR-1, and s-TFE were transduced with lentivirus expressing GFP, CRISPR-Cas9,
1110 and sgRNA (either control sgRNA (098) or sgRNA against TFE3). After 3 days, the GFP-positive rate was
1111 measured by a Fortessa flow cytometer to ensure it was higher than 90%. Seven days after viral infection, viral-
1112 infected cells were mixed with non-infected parental cells in a 1:1 ratio. Mixed cells were plated in 6-well
1113 plates. On days 3-24, cells were trypsinized and resuspended in 4% FACS buffer (FBS/PBS), and the GFP-
1114 positive rate was measured by a Fortessa flow cytometer. All flow cytometry data were analyzed with FlowJo
1115 (RRID:SCR_008520). GFP positive percentage in each condition at each time point was first normalized to
1116 value in that condition at d0, and then normalized to sgControl.

1117 **Colony Formation Assays**
1118 PC3, H460, Caki-1, 786-O, UOK109, UOK146, FU-UR-1, s-TFE, and ASPS-1 cell lines were transduced with
1119 lentivirus expressing CRISPR-Cas9 and sgRNA targeting the gene of interest, selected by puromycin, and then
1120 seeded in 12-well plates at various cell densities of 500-6,000 cells/well depending on the cell line. Media was
1121 replaced every 7 days. After 10-28 days, medium was aspirated, and cells were fixed and stained with 0.5%
1122 crystal violet in 25% (volume) methanol solution for about 15 minutes. Stained cells were washed with water
1123 and air-dried. Plates were scanned with an Epson scanner and quantified using ImageJ (RRID:SCR_003070).

1124 **Chronos Score Calculation**
1125 Log_2(fold-changes) in sgRNA abundance on day 28 of the screen were calculated using MAGeCK (130), using
1126 plasmid DNA as a reference. Exome sequencing data was aligned to hg38 using bwa mem (131), and copy-
1127 number was calculated using PureCN (132), as previously described (44). Chronos was used to normalize
1128 log_2(fold-changes) in sgRNAs with segmental copy-number correction (31). ccRCC cell lines were defined
1129 based on Cellosaurus NCIt disease type and included: OSRC2, CAKI2, SLR23, KMRC20, UOK101, SLR24,
1130 KMRC3, CAKI1, TUHR10TKB, SLR26, KMRC1, KMRC2 (RRID:CVCL_2984), SNU349, UMRC3, and RCCFG2.

1131 **Support Vector Regression Model**
1132 Model development and evaluation

1133 The DepMap (RRID:SCR_017655) 23Q2 expression matrix (converted to log_2(TPM+1), https://depmap.org) and
1134 23Q2 CRISPR-KO dependency score matrix (Chronos-normalized, https://depmap.org) were downloaded and
1135 subset to shared cell lines. We split these data into 5 equal subsets for 5-fold cross-validation (four training
1136 folds and evaluation on a validation fold). Expression was Z-scored for each gene. For each gene, a new model
1137 was trained to predict its dependency score.

1138 To reduce dimensionality, we first calculated the Pearson correlation coefficient between each feature (i.e. Z-
1139 scored gene expression) and the dependency score of the gene being analyzed in the training data. The top
1140 predictive features for each gene (ranked by absolute value of Pearson correlation coefficient, 5000 in final
1141 model [a number that we varied to maximize performance], see **Supplementary Fig. S3B**) were determined.

1142 For each gene, we subset the training data to these top features and trained a support vector regression model
1143 (sklearn.svm.SVR, RBF kernel) to predict dependency scores. We tested a variety of other models from sklearn
1144 including SVR with a linear kernel, ridge regression, lasso regression, elastic net, and k-nearest neighbors
1145 regression (**Supplementary Fig. S3B**). Performance on the validation fold was assessed by Pearson

correlation between predicted and observed (i.e. experimentally determined) Chronos scores for each gene across all cell lines in the validation fold. We repeated this process four more times (changing the validation fold) during cross-validation. Performance metrics were averaged between these five models for each gene. SVR with an RBF kernel had the best performance across all models tested with 657 genes being highly predictable (defined as R ≥ 0.4 between predicted and observed Chronos scores) (**Supplementary Fig. S3b**). The average Pearson correlation coefficient for predicted vs. observed Chronos score was R=0.16 across 16845 genes. The correlation between predicted and observed Chronos score across all gene-cancer cell line pairs in the test data was R = 0.92. Specifics and code for the developed pipeline as well as scripts for interactive visualization of predicted dependencies in this manuscript are available in Github: https://github.com/SViswanathanLab/TrPLet.

Model deployment

The models for each gene were retrained on the entire DepMap dataset prior to testing on external datasets. To calculate approximate coefficients from the model, we used a kernel trick taking the linear combination of support vector weighted by dual coefficients from RBF kernel. Broadly, our model was applied to three types of data: (1) TCGA tumor RNA-seq, (2) non-TCGA tumor RNA-seq, (3) cell line RNA-seq. (1) For TCGA tumor RNA-seq, we Z-scored the expression of each gene ($\log_2$(TPM+1)) within TCGA and predicted on the resulting normalized expression data. Clustering (two-component t-SNE) based on dependency scores (predicted: TCGA, experimentally-derived via CRISPR screen: DepMap) using this approach resulted in TCGA tumors clustering with screened cell lines from DepMap of the same lineage (see **Supplementary Fig. S6A**). (2) For non-TCGA tumor RNA-seq, we downloaded RNA-seq fastq files or count matrices when present, from the Gene Expression Omnibus (GEO; RRID:SCR_005012). Reads were aligned to GENCODE (RRID:SCR_014966) v38 transcript reference using STAR/RSEM (133,134). The resulting count matrices were inner joined with the TCGA count matrix (135) (https://osf.io/gqrz9/files/osfstorage), and batch corrected using ComBat-seq (136) using lineage as a covariate (for this purpose, tRCCs, Wilms' tumors, CDC, and RMC were classified as "KIRP"; ASPS, PEComa, and EHE were classified as "SARC"; ccRCC was classified as "KIRC"). The counts were then normalized to gene-level transcripts per kilobase million (TPM), converted to $\log_2$(TPM+1), and each gene's expression was then Z-scored (across the combined matrix consisting of the external dataset and TCGA). The resulting Z-scored expression in the external dataset was then used for prediction, as described above. (3) For cell line RNA-seq, a gene-level normalized expression matrix ($\log_2$(TPM+1)) was either downloaded or generated from STAR/RSEM. The expression of each gene in the resulting matrix was scaled (Z-scored) using the mean/standard deviation calculated when scaling the DepMap expression matrix. The resulting Z-scored expression values were used for prediction. Batch correction was forgone in this use-case based on tSNE clustering of tRCC cell lines with kidney cell lines in DepMap, and ASPS cell lines with soft tissue and CNS cell lines in DepMap based on expression profile (**Supplementary Fig. S6K**).

Survival Analysis

Count matrices from CM-025 (137) were used to predict MTOR dependency in ccRCC samples. Outcomes (overall survival, progression-free survival) between groups were compared using lifelines (138). Blinding, randomization not relevant to this study because analysis of these data was retrospective. Analyses were not stratified by sex as a biological variable.